CHAPTER 3

Comparative study on the reactivity of zero valent iron nanoparticles (Fe^0) and bimetallic iron-based nanoparticles for the removal of dyes and Cr(VI) from water

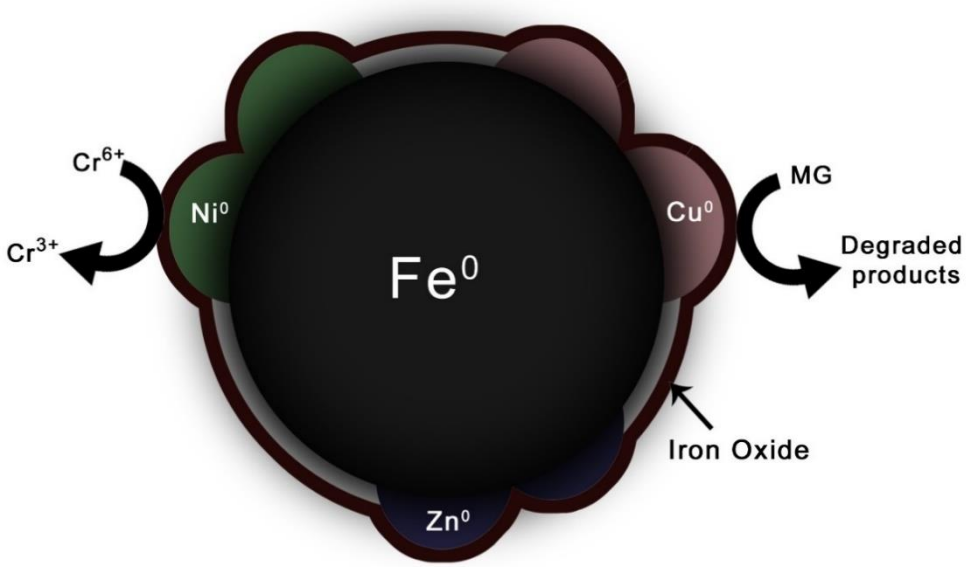

Chapter 3

Comparative study on the reactivity of zero valent iron nanoparticles (Fe^0) and bimetallic iron-based nanoparticles for the removal of Cr(VI) and dyes from water

3.1 Introduction

The high potential of Fe^0 nanoparticles for the remediation of water contaminants has been discussed thoroughly in chapter 1. Even though the Fe^0 nanoparticles show good efficiency for contaminant removal, the formation of the surface passive layer decreases the capacity of Fe^0 nanoparticles in the aqueous medium. Gradual reduction of reactivity over time, narrow pH range and low stability of the nanoparticles due to leaching are the additional drawbacks of monometallic nanoparticles. One of the efficient methods to overcome these problems and improve the efficiency of Fe^0 nanoparticles is incorporating a second metal on the surface of Fe^0 nanoparticles. The characteristics properties of bimetallic iron-based nanoparticles have differed from monometallic Fe^0 nanoparticles. The previous studies suggest that the iron-based bimetallic nanoparticles show high catalytic activity, increased selectivity, upgraded stability and less cost than monometallic Fe^0 nanoparticles. Iron-based bimetallic nanoparticles also followed adsorption, reduction, oxidation, including advanced oxidation mechanisms similar to Fe^0 nanoparticles in removing organic, inorganic and heavy metal contaminants from water and wastewater[1].

Generally, the preparation of bimetallic nanoparticles can be done through two methods - co-reduction and successive reduction of two metal salts. In the co-reduction method, two metal salts are mixed in a suitable solvent and simultaneously reduced using an appropriate reducing agent. It is similar to the preparation of monometallic nanoparticles. If the two metal ions have different redox potentials, the metal ion with the highest redox potential reduces fast, precipitates and forms the core and the second metal ion forms a shell on the core metal ion. If the two metal ions have similar redox potential, metal alloys will be formed due to simultaneous reduction. Successive reduction method is used to prepare core-shell bimetallic nanoparticles. At first, core metal nanoparticles are prepared through reduction using a potent reducing agent and then the second metal gets deposited on the surface of the core metal. This is due to the galvanic couple generated between the two

metals which in turn cause the reduction of the second metal by the core metal having a more negative reduction potential[2,3].

Bimetallic combinations such as Fe/Ni, Fe/Cu, Fe/Zn, Fe/Al and Fe/Ag were already reported earlier. However, the formation and reactivity towards contaminants are not established well. Tamer et al. compared the efficiency of Fe^0 and Fe/Cu nanoparticles to treat the radioactive caesium through adsorption. The result shows that the sorption process in Fe/Cu nanoparticles was kinetically faster and more efficient than in Fe^0. It is important to note that Fe^0 and Fe/Cu nanoparticles show high selectivity towards caesium in the presence of competing cations like Na^+, K^+, Ca^{2+} and Mg^{2+}[4]. Reductive detoxification of halogenated hydrocarbons, nitroaromatics and metalloids like Cr(VI) is a unique property of Fe^0. Bimetallisation of Fe^0 improves reduction capacity and prevents the formation of toxic byproducts. Fe^0 acts as the anode in dehalogenation reaction and gets oxidised, while the second metal catalyses electron transfer and hydrogen generation[5–7]. Tee et al. studied the role of Ni/Fe nanoparticles on the degradation of trichloroethylene. They found that Ni/Fe nanoparticles rapidly degraded the trichloroethylene and ethane was the main degradation product. They also noted that the Ni/Fe nanoparticles show a higher reaction rate than Fe nanoparticles and the degradation rate increases with an increase in Ni percentage from 2 wt % to 25 wt %. With the increase in nickel percentage, due to the formation of a less-reactive nickel-rich surface layer, the extent of trichloroethylene degradation gets decreases.

The degradation of p-nitrophenol using Fe/Cu nanoparticles under aerobic and anaerobic conditions was investigated by Xiong et al. Under anaerobic conditions, the reduction capacity of Fe/Cu bimetallic nanoparticles is higher than Fe^0 since the metal additives like Cu increase the steady-state concentration of atomic hydrogen at the surface or near-surface of the iron-based reductant and improves the electron transfer from Fe^0 to the pollutant resulting in the degradation of p-nitrophenol to p-aminophenol. Under the aerobic condition, the produced atomic hydrogen is consumed by the dissolved oxygen and decrease the reduction capacity of Fe/Cu nanoparticles. However, under aerobic conditions, the dissolved oxygen could be reduced into H_2O_2 by Fe^0 and these H_2O_2 provide hydroxyl radicals by the Fenton-like reaction. The strong oxidant, hydroxyl radical, could degrade the organic pollutant into mineralised form. They suggest that for Fe/Cu bimetallic nanoparticles, the aerobic condition would be the best method to treat pollutants since the Fe/Cu bimetallic nanoparticles not only break the benzene ring and

–NO_2 group of p-nitrophenol but also mineralised most of the intermediates into CO_2 and H_2O[8].

As previously mentioned, iron-based nanoparticles were used to treat water contaminants. In this study, dyes and hexavalent chromium were selected as model pollutants to examine the effectiveness of iron-based nanoparticles. Chromium naturally exists in the environment and it has many potential health risks for living organisms. Leather tanning, electroplating, painting and metallurgy industries use various forms of Cr as raw material[9]. Among the different oxidation states (-2 to +6), Cr(III) and Cr(VI) are the most commonly occurring oxidation states[10,11]. Cr(III) is an essential component for sugar and fat metabolism. Insufficient Cr(III) intake causes symptoms similar to diabetes and cardiovascular diseases[12]. A low Cr(III) concentration in plants promotes growth and increases yield. Cr(III) is more toxic than Cr(VI) due to its high oxidising potential, high solubility and mobility across the membranes in living organisms. Cr(VI) is carcinogenic and a powerful epithelial irritant. Cr(VI) also affects humans' well-being by causing diseases such as liver damage, pulmonary congestion, vomiting, and severe diarrhoea[13]. It is also noted that Cr(VI) is toxic to aquatic organisms and plants. Usually, Cr(VI) is seen in the environment as chromate (CrO_4^{2-}), dichromate ($Cr_2O_7^{2-}$) and CrO_3, while Cr(III) is seen as oxides, hydroxides and sulphates which are less toxic, relatively insoluble in water, exhibit less mobility and shows a high tendency to bound to organic matter. Cr(III) forms hydroxide and precipitates with Fe in ground water[14]. Nevertheless, in the presence of high concentrations of oxygen or oxides of Mn, the Cr(III) can be oxidised to Cr(VI)[15].

Dyes are a noteworthy class of organic compounds used in the textile, paper, cosmetic and food industries. Many dyes and their degradation products are toxic, mutagenic and carcinogenic to living organisms. They reduce sunlight penetration, leading to the decreased photosynthetic activity of the aquatic life even at low concentrations. So, the treatment of dye-containing water is necessary before releasing them into the environment[16]. Malachite green (MG) is a basic, cationic triphenylmethane dye produced by the polymerisation of benzaldehyde and dimethylaniline in the presence of concentrated sulphuric acid. In aquaculture, MG is used as an insecticide and fungicide. It is also used as a dye in the silk, wood, cotton, leather, paper and acrylic industries due to its low cost, good efficiency, lack of suitable alternatives and easy availability. MG has a complex aromatic structure which may cause its degradation problematic. MG decreases

the sunlight penetration in the water bodies, affecting the photosynthetic activity and productivity of the aquatic system. MG is environmentally persistent and shows teratogenic, mutagenic and carcinogenic effects. It may cause detrimental effects in the liver, gill, kidney, intestine and gonads in aquatic organisms. In humans, it may cause tumours by inhibiting human glutathione-S-transferase activity and irritating the gastrointestinal tract due to ingestion. Skin contact with MG causes irritation, pain and redness. The adverse effects of MG make its effective removal mandatory[17–19].

Methyl blue (MB) is an anionic triphenylmethane dye used as a biological colouring agent and pH indicator. It is also applied for leather and cotton. MB dye is harmful if swallowed and lead to skin, eye and respiratory tract irritation. As per literature, very little study has been reported about the toxicity and removal of MB from aqueous media[20,21]. Methyl orange (MO) is an anionic azo dye commonly applied in chemical, textile and paper industries. It has a mono-azo bond and the sulphonic and azo groups present in the molecular structure cannot be degraded easily, which harms the environment. It is poisonous when swallowed and causes allergic reactions like skin eczema if contacted to the skin[22–25]. Methylene blue (MLB) is a cationic thiazine dye generally used in paper, textile and dye industries. It will cause nausea, vomiting and diarrhoea when ingested through the mouth[26,27]. The detrimental effects of dyes make it a great concern from an environmental and healthy point of view.

Although many researchers investigated the effectiveness of bimetallic iron-based nanoparticles, there is a lack of information about Cr(VI) reduction and dye degradation. This study examined the most effective bimetallic combination and the optimum percentage of the second metal deposition. The objectives of this study are (i) synthesis of Fe^0 nanoparticles and bimetallic Fe based nanoparticles, (ii) characterisation of the prepared nanoparticles by HRTEM, XRD and EDAX (iii) optimisation of second catalytic metal loaded on the Fe^0 nanoparticles, (iv) determine the effectiveness of prepared nanoparticles for the decolourisation of four different dyes and hexavalent chromium (v) investigate the effect of various parameters including nanoparticle dosage, initial concentration of pollutant, solution pH and the contact time in pollutant removal (vi) to find out the MG degradation mechanism through analysing the degradation products.

3.2 Experimental details

3.2.1 Synthesis of Fe^0, Fe/Ni, Fe/Cu and Fe/Zn nanoparticles

Monometallic Fe^0 and bimetallic Fe/Ni, Fe/Cu and Fe/Zn nanoparticles were prepared by the liquid-phase reduction method under nitrogen atmosphere using sodium borohydride as the reducing agent. Ferric solution is prepared by dissolving 1 g of $FeCl_3.6H_2O$ in 10 mL ethanol-water (1:1) solution and stirred for 15 minutes under the nitrogen atmosphere. Sodium borohydride (0.5 g) was dissolved in 50 mL water and added dropwise to ferric chloride solution. The appearance of a black precipitate indicates the formation of Fe^0 nanoparticles (as shown in equation 3.1) which was then collected through vacuum filtration. After washing with ethanol, the nanoparticles were lyophilised and stored in airtight bottles. Figure 3.1 show the preparation of Fe^0 nanoparticles using $NaBH_4$.

$$2FeCl_3 + 6NaBH_4 + 18H_2O \rightarrow 2Fe^0 + 6B(OH)_3 + 6NaCl + 21H_2 \uparrow \qquad (3.1)$$

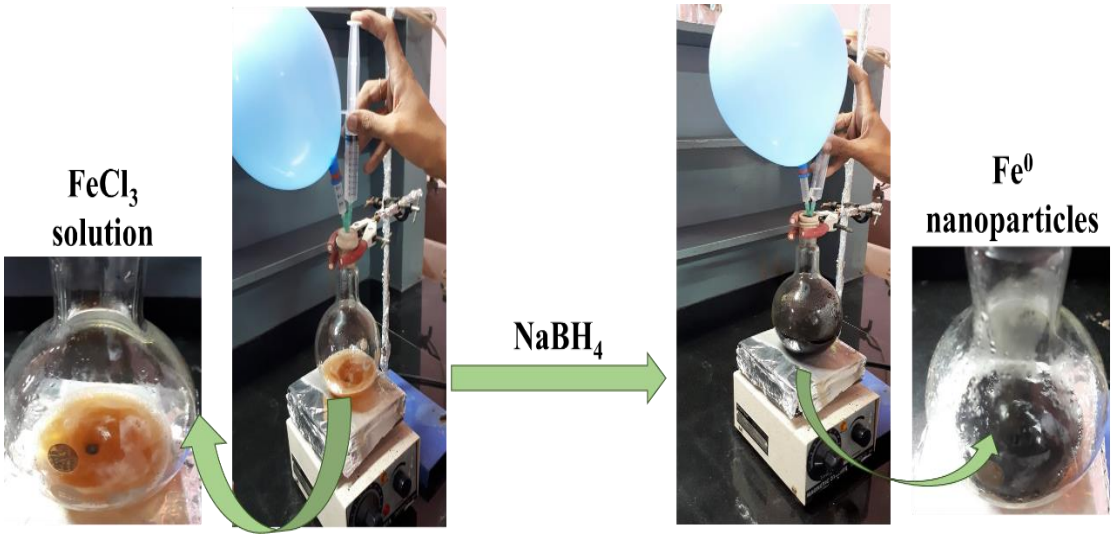

Figure 3.1 *Photographs of the preparation of Fe^0*

The method for preparing bimetallic nanoparticles was similar to the monometallic synthesis. In the preparation of Fe/Cu and Fe/Ni bimetallic nanoparticles, 10 mL metal salt solutions of either $NiSO_4.6H_2O$ or $CuSO_4.5H_2O$ of specific concentration were prepared and added dropwise to the freshly prepared iron particle suspended in absolute ethanol. The solution is rapidly stirred for 30 minutes to achieve bimetallic nanoparticles with specific second metal loading. Fe/Zn nanoparticles were prepared by the co-reduction method by mixing solutions with a specific concentration of $FeCl_3.6H_2O$ and $Zn(NO_3)_2.6H_2O$ and reducing them simultaneously under the nitrogen atmosphere. The prepared bimetallic nanoparticles were vacuum filtered, lyophilised and stored in airtight

bottles. Bimetallic nanoparticles with 5, 10 and 15 weight % of second metal were prepared by changing the concentration of the second metal salt solution. The reaction of Fe^0 with $Ni^{2+}$and Cu^{2+} is shown in equations 3.2-3.3.

$$Ni^{2+} + Fe^0 \rightarrow Ni^0 + Fe^{2+} \quad (3.2)$$

$$Cu^{2+} + Fe^0 \rightarrow Cu^0 + Fe^{2+} \quad (3.3)$$

3.2.2 Batch experiments

Cr(VI) removal studies

The method followed for the batch experiments of Cr(VI) removal were already given in chapter 2. In the present study, various parameters investigated for the removal of Cr(VI) are nanoparticle dosage (1-8 g/L), initial concentration of Cr(VI) (1-7 mg/L), initial pH of the solution (4-10) and contact time (5-20 min). 1.0 M NaOH and 1.0 M H_2SO_4 were used to adjust the pH of the solution. All experiments were performed with a duplicate.

Dye removal studies

Malachite green (MG), methyl blue (MB), methylene blue (MLB) and methyl orange (MO) dye solutions were prepared by dilution of stock solution just before use. Dye removal experiments were carried out in 100 mL beakers with 20 mL of dye solution. Firstly, 0.5 g/L of nanoparticles were added to the 50 mg/L of the dye solution in a beaker and rapidly agitated using a bath sonicator. The samples were collected after 15 minutes and the absorbance was measured using a UV-visible spectrophotometer. Samples without the addition of nanoparticles have been examined under identical conditions and no significant changes were observed. The MG dye removal was investigated thoroughly by changing nanoparticles dosage (0.25–1 g/L), initial concentration of the dye (10–50 mg/L), pH (5-7) and contact time (5-30 min). To study the effect of pH, the initial pH of the dye solution was adjusted using 1.0 M NaOH and 1.0 M H_2SO_4. All experiments were performed with a duplicate.

3.2.3 Characterisation and analytical techniques used

The prepared nanoparticles were characterised by HRTEM, EDAX and XRD techniques. Details of characterisation techniques are discussed in chapter 2. Elemental analysis and mapping of the Fe^0, Fe/Ni, Fe/Cu and Fe/Zn nanoparticles were done by EDAX (Jeol 6390LA/OXFORD XMX N). EDAX analysis using Bruker Nano GmbH, XFlash detector

6/100 were done to find out the presence of chromium in Fe^0, Fe/Ni, Fe/Cu and Fe/Zn nanoparticles which is treated with the hexavalent chromium solution. The degradation products of MG dye was analysed by LC-MS/MS and GC-MS/MS. The aqueous solution of MG dye after treating with Fe^0 nanoparticles was collected, filtered through a 0.22 µm membrane filter and divided into two equal volumes. The first part is used for LC-MS/MS analysis and the second part was used for GC-MS/MS analysis.

To determine the volatile MG degradation products in the solution using GC-MS/MS, the samples were centrifuged at 5000 rpm for 15 minutes and the supernatant solution was extracted twice with ethyl acetate (10 mL). Then the extract was concentrated to 1 mL and filtered using a 0.22 µm syringe filter. Gas chromatography coupled with triple quadrupole tandem mass spectrometry (GC-MS/MS) analysis of the MG dye degradation products were carried out using TSQ 8000 GC-MS/MS. The separation of compounds has been done using the DB-5MS capillary column (30 m × 0.25 mm × 0.25 µm). The carrier gas was helium with a flow rate of 1mL/min. The column oven temperature was programmed from an initial temperature of 40ºC (hold 1 min) to 100ºC (hold 1 min) then to 150 ºC (hold 1 min) and finally to 250ºC (hold 1 min) each at 10ºC min^{-1}. The injection volume was 1 mL and the oven running time was 25 minutes. The ionisation energy applied was 70 eV. Data acquisition was started after a solvent delay of 4 minutes, with the mass spectrometer operating in full-scan mode. Compounds were identified using the National Institute of Standards and Technology (NIST) MS search 2.0 Library.

The MG dye degradation products identification was also carried out on an LC-MS/MS system. Liquid chromatography was performed using a Dionex Ultimate 3000 (Thermo) micro-LC equipped with C18, 150 x 4.6 mm, 5 µm reversed-phase column operated at 25ºC. The UV detection wavelength was 254 nm. The mobile phase consisted of water (A) and acetonitrile (B) containing 0.1 % formic acid. The gradient program was (time (min), % B): (0.00, 1); (5.00, 1); (30.00, 20); (45.00, 40); (60.00, 95); (74.00, 95); and (75.00, 1) and the flow rate was 300 µL/min. Impact HD (Bruker) ESI QTOF high-resolution mass spectrometer was used for MS/MS analysis in the positive ions mode and the mass range was 100-2000 m/z. The ESI conditions were as follows: capillary voltage, 4500 V; the nebuliser pressure, 60 psi; drying gas flow, 12 L min^{-1}; temperature, 220 °C.

3.3 Results and discussion

3.3.1 Characterisation of Fe^0, Fe/Ni, Fe/Cu and Fe/Zn nanoparticles

HRTEM

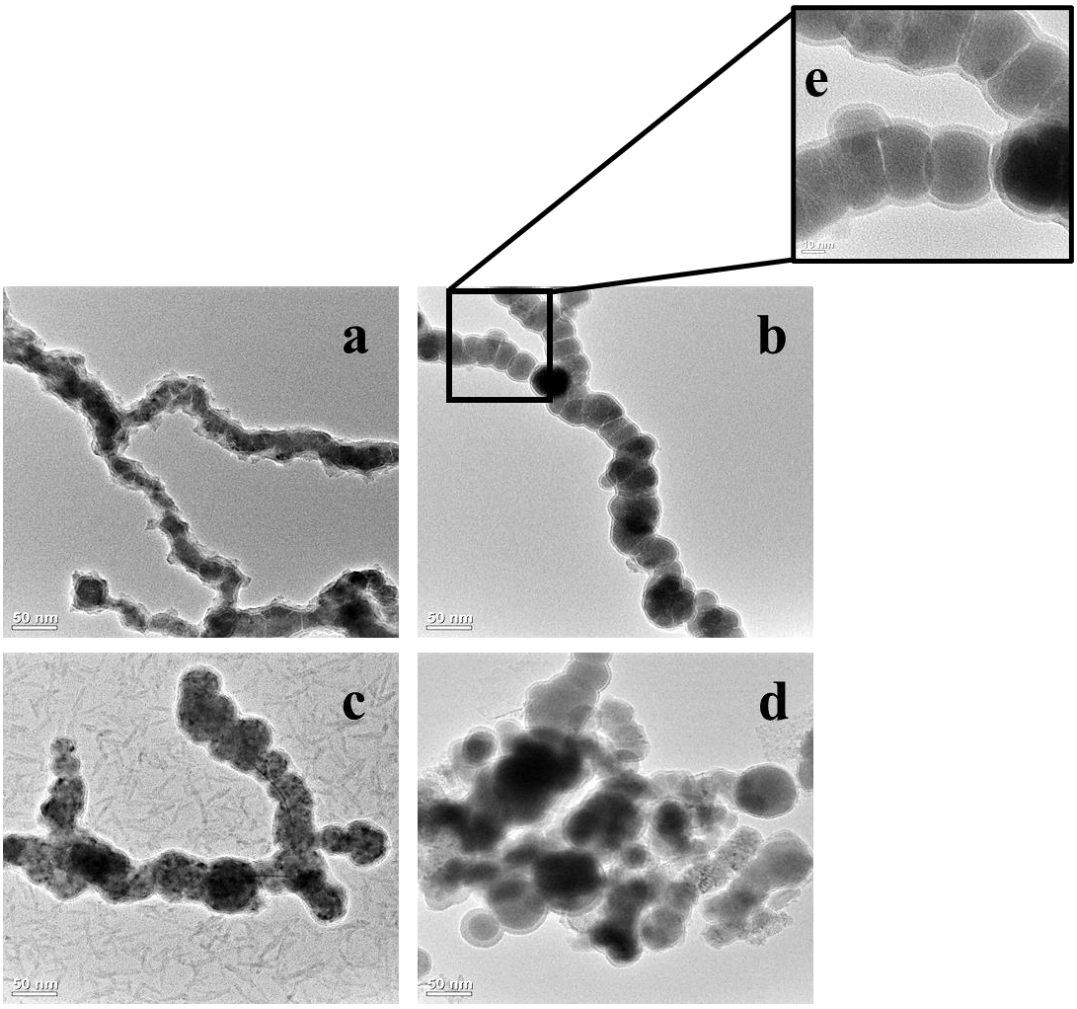

Figure 3.2 *HRTEM images of a) Fe^0 b) Fe/Cu c) Fe/Ni d) Fe/Zn nanoparticles and e) HRTEM image of Fe/Cu nanoparticles enlarged.*

Figure 3.2 shows the HRTEM images of monometallic Fe^0 nanoparticles and bimetallic Fe/Cu, Fe/Ni and Fe/Zn nanoparticles. All the prepared nanoparticles show a tendency for agglomeration, primarily as chain clusters due to the electrostatic and magnetic interactions. The dark colour in the HRTEM image indicates the heavier atomic mass/high-density particles and the bright colour indicates the lighter atomic mass/low-density particles. The results show that the major composition of the prepared nanoparticles has a core of highly dense Fe^0 particles and a shell of low dense iron oxides. The structure of bimetallic nanoparticles is complicated and varies from core-shell segregated structures to intermetallic/alloyed structures. The characteristics of the second

metal do not significantly influence the morphology of the nanoparticles. Two factors influencing the bimetallic formation are the surface energies of the metals involved and the atomic radii of the metals. The element with low surface energy is deposited on those with high surface energy. The particle size distribution of prepared nanoparticles is shown in table 3.1.

Nanoparticle	Particle size range	Average particle size
Fe^0	21.9 - 45 nm	30.9 nm
Fe/Cu	14.4 – 50.2 nm	37.0 nm
Fe/Ni	17.7 - 71.0 nm	41.8 nm
Fe/Zn	19.2 - 85.7 nm	43.2 nm

Table 3.1 *Average particle size and particle size distribution of Fe^0, Fe/Ni, Fe/Cu and Fe/Zn nanoparticles*

The selected area electron diffraction (SAED) pattern of the prepared nanoparticles is shown in figure 3.3. The SAED pattern shows that the particles have crystalline and amorphous nature. The bright spots in the SAED pattern indicate the crystalline nature of Fe^0 and bimetal whereas the faded rings indicate the presence of amorphous iron oxide particles.

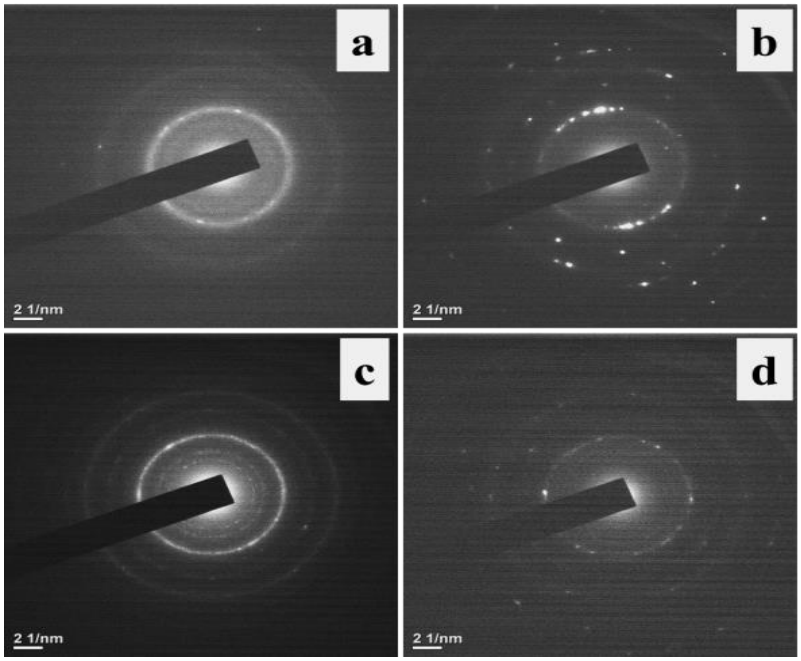

Figure 3.3 *SAED pattern of a) Fe^0 b) Fe/Cu c) Fe/Ni and d) Fe/Zn nanoparticles*

XRD

Figure 3.4 (a, b, c & d) shows the XRD pattern of Fe^0, Fe/Ni, Fe/Cu and Fe/Zn nanoparticles prepared by chemical reduction method. All the samples exhibit the characteristic peak of Fe^0 and peaks due to the formation of iron oxides. In Fe^0 nanoparticles, the peak at 44.7º corresponds to the (110) plane of Fe^0[28]. The peak at 31.51º matched with the (210) plane of γ-FeO(OH)[29] and the peak at 34.95º confirmed the presence of Fe_2O_3 ((201) plane)[30]. In the case of bimetallic nanoparticles, there was a shift in the characteristic peak of the Fe^0. The prepared Fe/Ni, Fe/Cu and Fe/Zn bimetallic nanoparticles exhibit the characteristic peak of Fe^0 at 44.9º, 45.1º and 45.2º respectively. It may be due to the stress-induced deviation due to nickel, copper or zinc deposition over the template Fe^0 nanoparticles. However, the weight percentage of the second metal loaded on the Fe^0 nanoparticles was too low to detect any characteristic peak of Cu, Ni or Zn. The peaks due to the oxidation of Fe^0 nanoparticles were seen in the XRD spectra of prepared nanoparticles. The peaks at 30.5º and 35.2º correspond to the (220) and (311) planes of Fe_3O_4[31]. In addition, impurities due to the addition of reducing agent $NaBH_4$ were causing some peaks in the XRD spectra of prepared nanoparticles.

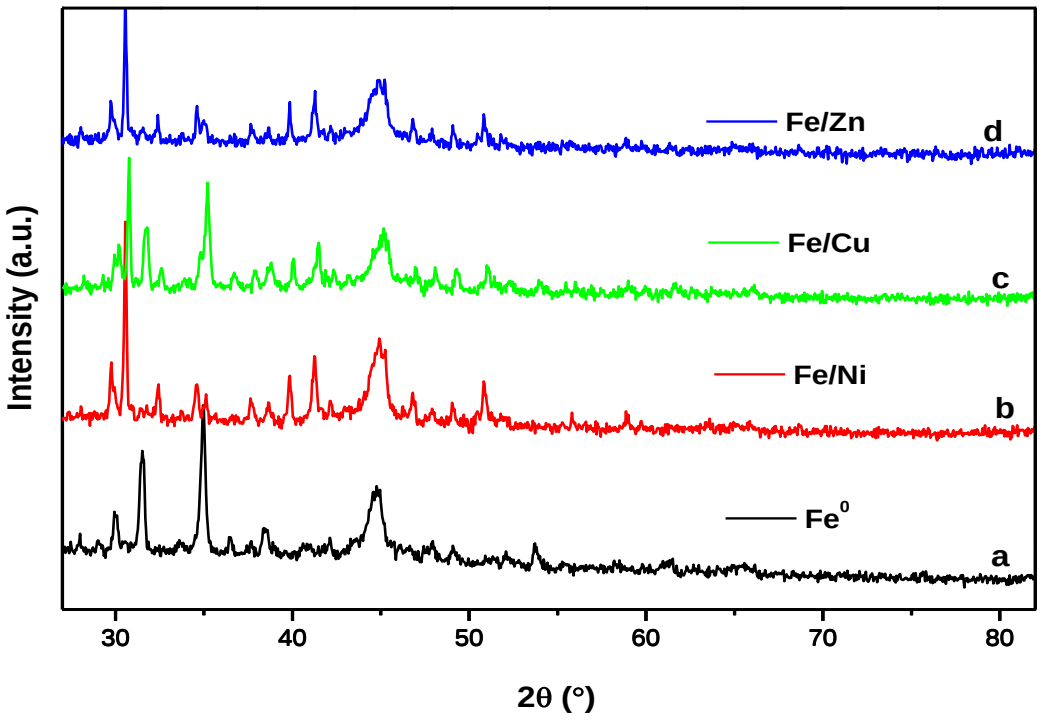

Figure 3.4 *XRD pattern of (a) Fe^0, (b) Fe/Ni, (c) Fe/Cu and (d) Fe/Zn nanoparticles*

EDAX

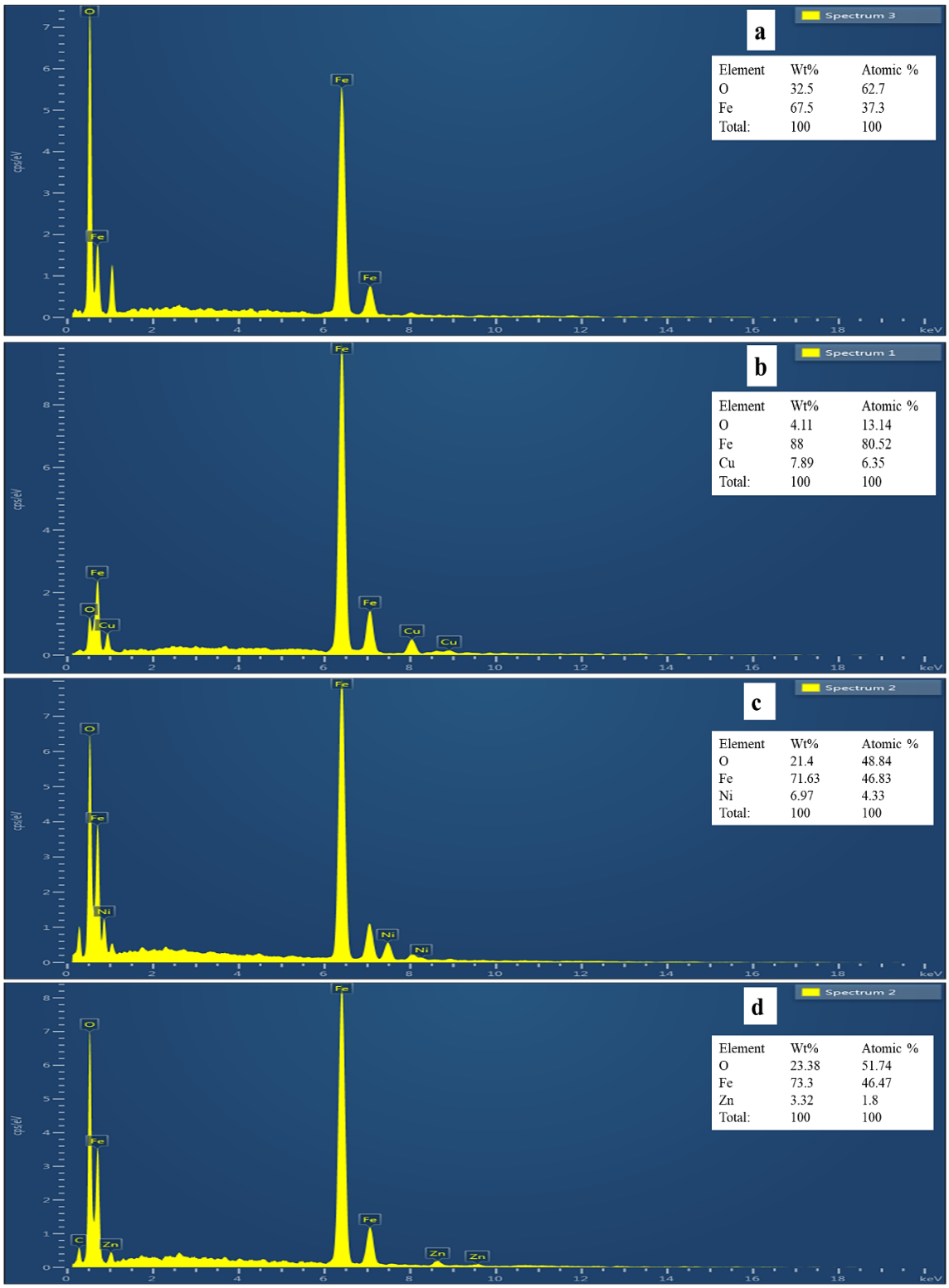

Figure 3.5 *EDAX spectra of (a) Fe^0, (b) Fe/Cu, (c) Fe/Ni and (d) Fe/Zn nanoparticles*

EDAX was used to analyse the elemental composition of Fe, O and second metal (Cu, Ni and Zn) in the prepared nanoparticles composition. As shown in figure 3.5, the weight percentages of 7.89 % (Cu), 6.97 % (Ni) and 3.32 % (Zn) of second metal successfully plated on the surface of the iron nanoparticles. The weight % of the second metal in Fe/Zn is less compared to other bimetallic nanoparticles. The presence of O in the nanoparticles indicates that the prepared nanoparticles tend to form metal oxide by contact with the air. Compared to monometallic nanoparticles, the weight percentage of oxygen is less in bimetallic nanoparticles. It indicates that the addition of second metal on the surface of Fe^0 reduce the rapid oxidation of Fe^0 nanoparticles.

3.3.2 Cr(VI) removal studies

Cr(VI) removal efficiency of Fe^0 and bimetallic nanoparticles has been studied using 5 mg/L Cr(VI) solution and depicted in figure 3.6. The UV-visible spectra of the removal study show that Fe/Ni nanoparticles exhibit the highest removal efficiency followed by Fe/Cu, Fe^0 and Fe/Zn nanoparticles respectively. Figure 3.7 represents the Cr(VI) removal photographs using prepared nanoparticles.

Typically Fe^0 exhibits three mechanisms for removing Cr(VI) - reduction, adsorption and co-precipitation. During the reduction process, Cr^{6+} was reduced into Cr^{3+} and precipitated as $Cr(OH)_3$ as represented by equations 3.4 and 3.5.

$$2Fe^0 + Cr_2O_7^{2-} + 8H^+ \longrightarrow 3Fe^{2+} + 2Cr(OH)_3 + H_2O \quad (3.4)$$

$$6Fe^{2+} + Cr_2O_7^{2-} + 8H^+ \longrightarrow 6Fe^{3+} + 2Cr(OH)_3 + H_2O \quad (3.5)$$

The reduced Cr^{3+} also form mixed Cr^{3+}–Fe^{3+} hydroxides by reacting with Fe^{3+} and H_2O represented in equations 3.6 and 3.7.

$$xCr^{3+} + (1-x)Fe^{3+} + 3H_2O \rightarrow Cr_xFe_{1-x}(OH)_3 + 3H^+ \quad (3.6)$$

$$xCr^{3+} + (1-x)Fe^{3+} + 2H_2O \rightarrow Cr_xFe_{1-x}OOH + 3H^+ \quad (3.7)$$

Along with this, the FeO(OH) formed by reacting the $Fe^{2+/3+}$ with water molecules acted as a suitable adsorbent for Cr(VI). The formation of the oxide/hydroxide layer of Fe along with the Cr species causes self-inhibition of electron transfer from Fe^0 to Cr(VI) and eventually leads to the shortfall in the reductive precipitation of Cr(VI)[2].

The prepared Fe/Ni and Fe/Cu bimetallic nanoparticles show better efficiency than Fe^0 and Fe/Zn. It is probably due to more reductive precipitation of Cr(VI) since

bimetallisation of Fe^0 nanoparticles improves the electron transfer of Fe^0 core to the Cr(VI). During the iron corrosion of bimetallic nanoparticles, molecular hydrogen formed on the surface of catalytic metal along with ferrous iron production. Cr(VI) was adsorbed onto the surface of Fe/Ni and Fe/Cu nanoparticles and reduced by the electron transfer from Fe or second metal (Ni or Cu). The decreased efficiency of Fe/Zn nanoparticles owing to the rapid oxidation of the Zn due to their high reactivity[32].

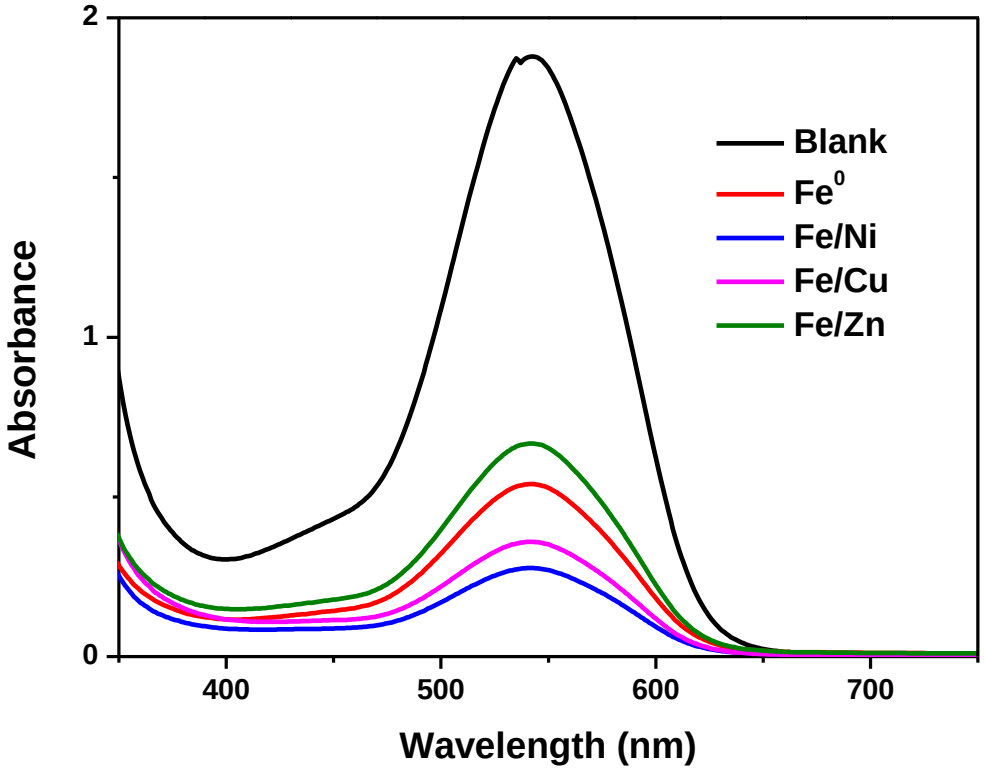

Figure 3.6 *UV-visible spectra of Cr(VI) after treating Fe^0, Fe/Ni, Fe/Cu and Fe/Zn nanoparticles*

Figure 3.7 *Photographs of Cr(VI) removal using Fe^0, Fe/Ni, Fe/Cu and Fe/Zn nanoparticles*

EDAX analysis

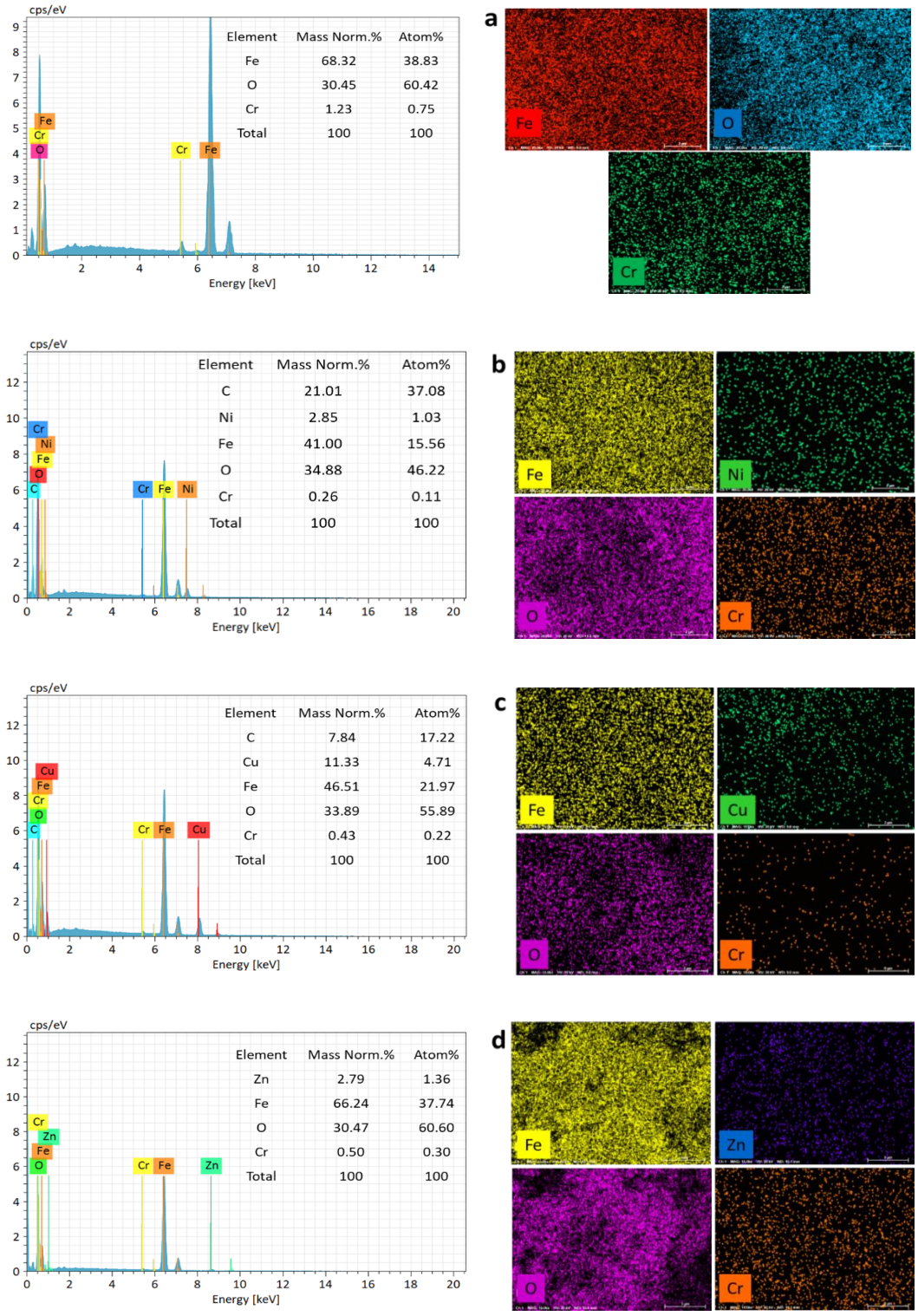

Figure 3.8 *EDAX spectra and mapping of (a) Fe^0, (b) Fe/Ni, (c) Fe/Cu and (d) Fe/Zn nanoparticles after treating with Cr(VI) solution*

The precipitation of Cr(VI) on the surface of Fe^0 and bimetallic nanoparticles were further confirmed by EDAX. Figure 3.8 shows the EDAX spectra and mapping of Fe^0, Fe/Ni, Fe/Cu and Fe/Zn nanoparticles after reacting with Cr(VI) solution. All the samples show a significant amount of Cr, which confirms the precipitation of Cr(VI) on the surface of prepared nanoparticles. It was also observed from the mapping image that all the elements are homogeneously distributed in the matrix.

Effect of the nanoparticle dosage

The influence of nanoparticle dosage on Cr(VI) removal was examined using different nanoparticles dosage (1-8 g/L), keeping the initial Cr(VI) concentration (5 mg/L) and contact time (10 min) as constant. As shown in figure 3.9a, the higher nanoparticle dosage lowers the Cr(VI) concentration in the solution. Fe/Ni nanoparticles have shown the highest removal efficiency and the lowest by Fe/Zn nanoparticles. Fe/Ni nanoparticles attained 88 % removal efficiency using a nanoparticle dosage of 2 g/L. At the same time, Fe/Cu, Fe^0 and Fe/Zn show 83 %, 73 % and 66 % Cr(VI) removal efficiency only. It is important to note that all the samples attained 100 % removal efficiency while using a nanoparticle dosage of 8 g/L. As the dosage of nanoparticles increases, there will be an increase in the number of reactive sites for Cr(VI). It will eventually lead to more reduction and adsorption[33].

Effect of the initial concentration

Figure 3.9b shows the effect of the initial concentration of Cr(VI) on the removal of Cr(VI) from water at constant contact time (10 min) and nanoparticles dosage (2 g/L). The initial Cr(VI) concentration varies from 1 to 7 mg/L. As expected, Cr(VI) removal efficiency increases with a decrease in the initial concentration of Cr(VI). All the nanoparticles show 100 % removal efficiency at 1 mg/L solution. But in the initial concentration of 7 mg/L, the nanoparticles show 71 %, 65 %, 61 % and 56 % removal efficiency for Fe/Ni, Fe/Cu, Fe^0 and Fe/Zn nanoparticles respectively. The binding sites available for Cr(VI) removal were fixed at a definite amount of nanoparticles dosage. As the concentration increases, the insufficient availability of reactive sites decreases the Cr(VI) removal. Along with that, the rapid formation of Fe^{3+}-Cr^{3+} hydroxide on the surface of nanoparticles suppresses the Cr(VI) reduction in higher Cr(VI) concentration[33].

Effect of contact time

The effect of contact time on the removal of Cr(VI) has been studied by keeping nanoparticles dosage (2 g/L) and initial concentration of Cr(VI) (5 mg/L) as constant. Fe/Ni nanoparticles completely removed Cr(VI) from the solution within 20 minutes of reaction time. As indicated in figure 3.9c, Cr(VI) removal efficiency was maximum in the first 15 minutes, which may be attributed to the presence of enormous available binding sites for Cr(VI). After 15 minutes of contact time, the nanoparticles slightly move to the equilibrium state owing to the decrease in the vacant binding sites and precipitation of Fe^{3+}-Cr^{3+} hydroxide on the surface of nanoparticles[34].

Effect of pH

One of the significant parameters influencing the effective removal of Cr(VI) is the pH of the solution. In this study, the influence of the solution pH 4, 7 and 10 has been studied (figure 3.9d) by taking other parameters such as initial Cr(VI) concentration (5 mg/L), contact time (10 min) and nanoparticle dosage (2 g/L) as constant. The results show that all the nanoparticles show 100 % removal efficiency at pH 4. When the pH of the solution increases, different nanoparticles show different Cr(VI) removal capacities. Under neutral pH, Fe/Ni nanoparticles show the highest removal efficiency followed by Fe/Cu, Fe^0 and Fe/Zn nanoparticles. Fe/Ni and Fe/Cu nanoparticles show higher removal efficiency at pH 10 than Fe^0 nanoparticles and Fe/Zn nanoparticles. Fe/Zn nanoparticles are drastically influenced by the pH of the solution and reduce its efficiency to 34 % at pH 10.

The high removal efficiency of Cr(VI) at low pH is attributed to the electrostatic attraction between negatively charged Cr(VI) anions with the positively charged nanoparticle surface. The formed passive iron oxide layer due to the oxidation is effortlessly removed at low pH. This creates more reactive sites for Cr(VI) reduction and adsorption. Along with that at acidic pH, the predominant Cr(VI) species present in the solution was $HCrO_4^-$ which is more susceptible for adsorption compared with CrO_4^{2-}. In higher pH, the prevalent Cr(VI) forms are CrO_4^{2-} and $Cr_2O_7^{2-}$. Electrostatic repulsion and competition between Cr(VI) anions and OH^- ions are the major reasons behind the less removal of Cr(VI) at higher pH[32–35].

Effect of second metal deposition on Fe^0

Effect of second metal loading on the removal of Cr(VI) has been studied (as shown in figure 3.9e) by keeping all other parameters such as initial Cr(VI) concentration (5 mg/L), nanoparticle dosage (2 g/L) and contact time (10 min) constant. The results inferred that Fe/Ni nanoparticles are highly reactive than Fe/Cu and Fe/Zn bimetallic nanoparticles. The optimum bimetal percentage for the better Cr(VI) removal was 10 %. At 15 % of bimetal concentration, the Cr(VI) removal efficiency does not significantly improve compared to 10 % second metal loading.

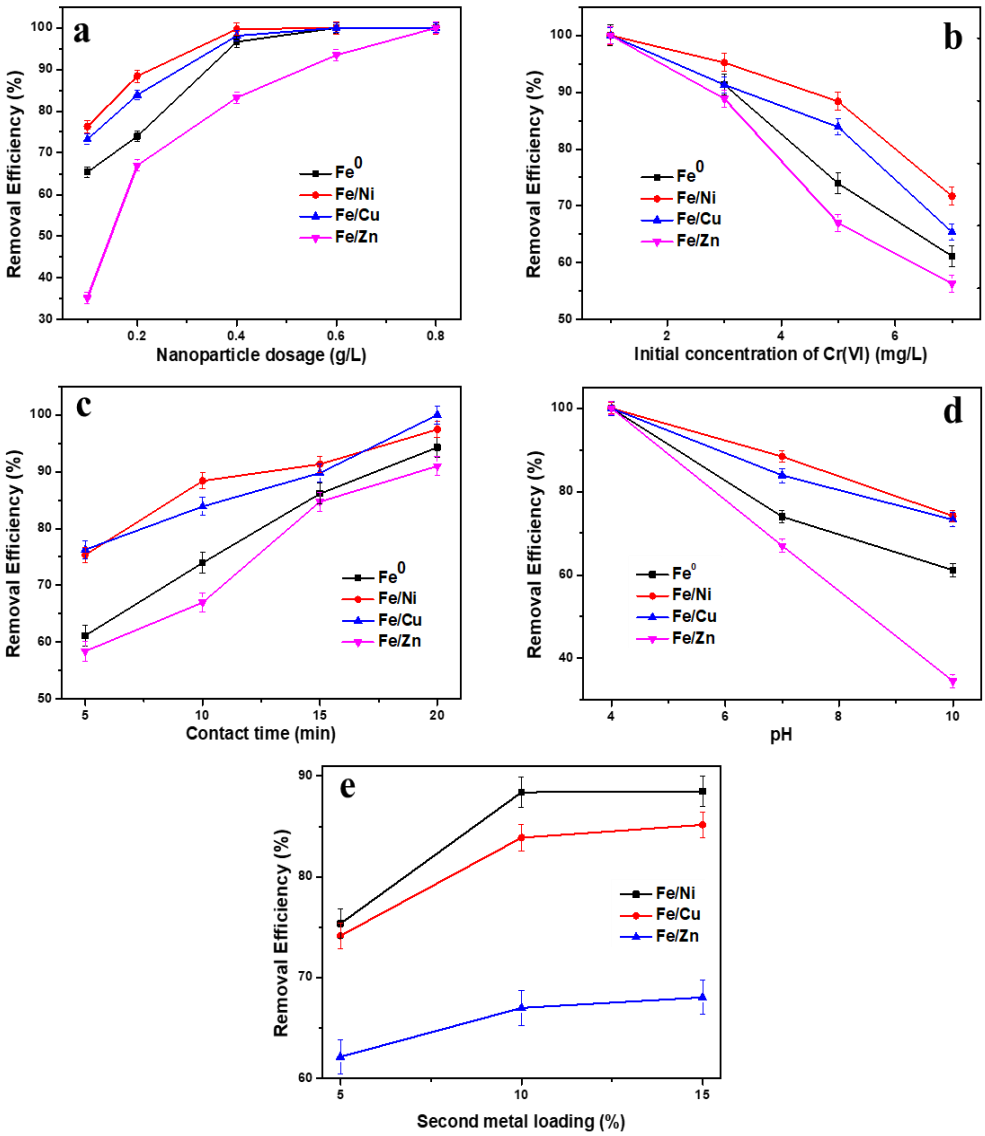

Figure 3.9 *(a) Effect of nanoparticle dosage (b) Effect of initial concentration of Cr(VI) (c) Effect of contact time (d) Effect of pH (e) Effect of second metal loading in Cr(VI) removal using Fe^0, Fe/Ni, Fe/Cu and Fe/Zn nanoparticles*

3.3.3 Dye removal studies

Effect on different dyes

As shown in figure 3.10, four commonly used organic dyes (MG, MB, MO and MLB) were used to check the reactivity of Fe^0 and three bimetallic nanoparticles (Fe/Ni, Fe/Cu and Fe/Zn). In the decolourisation experiment, the 50 mg/L of freshly prepared dye solutions were treated with 0.8 g/L of nanoparticles for 15 minutes. It was observed that Fe/Cu and Fe/Ni bimetallic nanoparticles show better removal efficiency compared to Fe^0 and Fe/Zn nanoparticles. It was noteworthy that the iron-based nanoparticles effectively removed cationic and anionic triphenylmethane dyes compared to azo or thiazine dyes. It may be due to the differences in structure and functional groups of dyes.

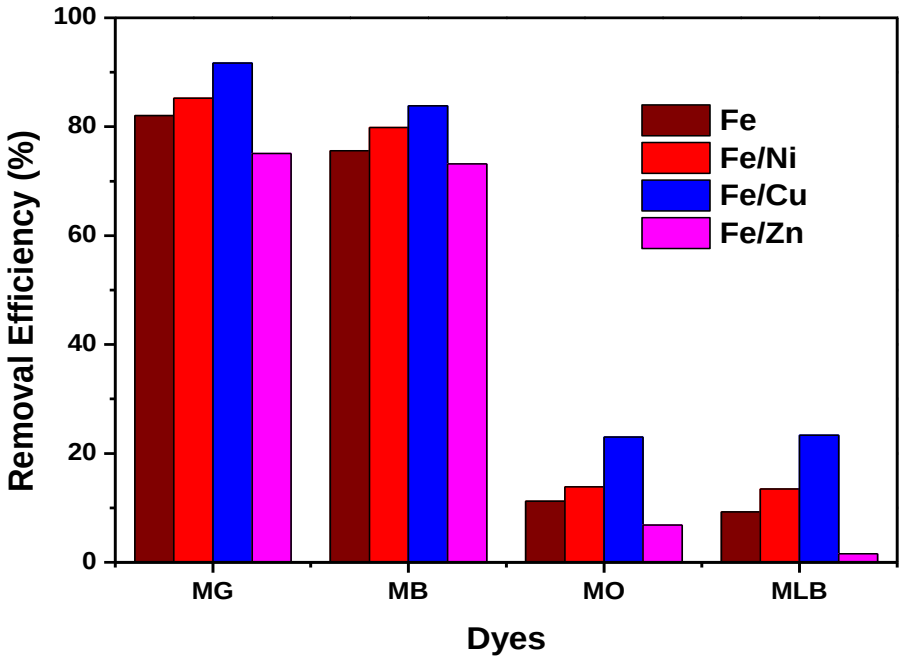

Figure 3.10 *Comparison of percentage removal of MG, MB, MO and MLB dyes using Fe^0, Fe/Ni, Fe/Cu and Fe/Zn nanoparticles*

MG removal using Fe^0, Fe/Ni, Fe/Cu and Fe/Zn nanoparticles

MG was selected as a model pollutant among four different dyes to study the effect of different parameters on iron-based nanoparticles. Figure 3.11 demonstrates the UV-visible spectra of MG after reacting with iron-based nanoparticles and figure 3.12 represents the corresponding reaction photographs. The characteristic peak of MG was observed at 617 nm, which corresponds to the -C-N- functional groups of MG. The absorptions observed at 424 nm, 316 nm and 248 nm are due to the conjugated framework of MG comprising

of aromatic rings. After adding iron-based nanoparticles, the peaks at 617 nm, 424 nm and 316 nm were alarmingly decreased and a new peak emerged at 360 nm. The emergence of a new peak indicated the degradation of the MG dye molecule. According to Du et al, the peak at 360 nm confirms the presence of 4-dimethylamino benzophenone, a significant degradation product formed by the attack on the central carbon of MG. The peak at 248 nm corresponds to the single benzene absorption, which is enhanced after the addition of iron-based nanoparticles and it also suggests the degradation of the MG dye molecule[18]. Fe/Cu shows the highest removal efficiency among the four iron-based nanoparticles followed by Fe/Ni, Fe^0 and Fe/Zn nanoparticles. Better electron transfer and production of reactive oxygen species could be the reason for enhanced decolourisation of MG dye solution.

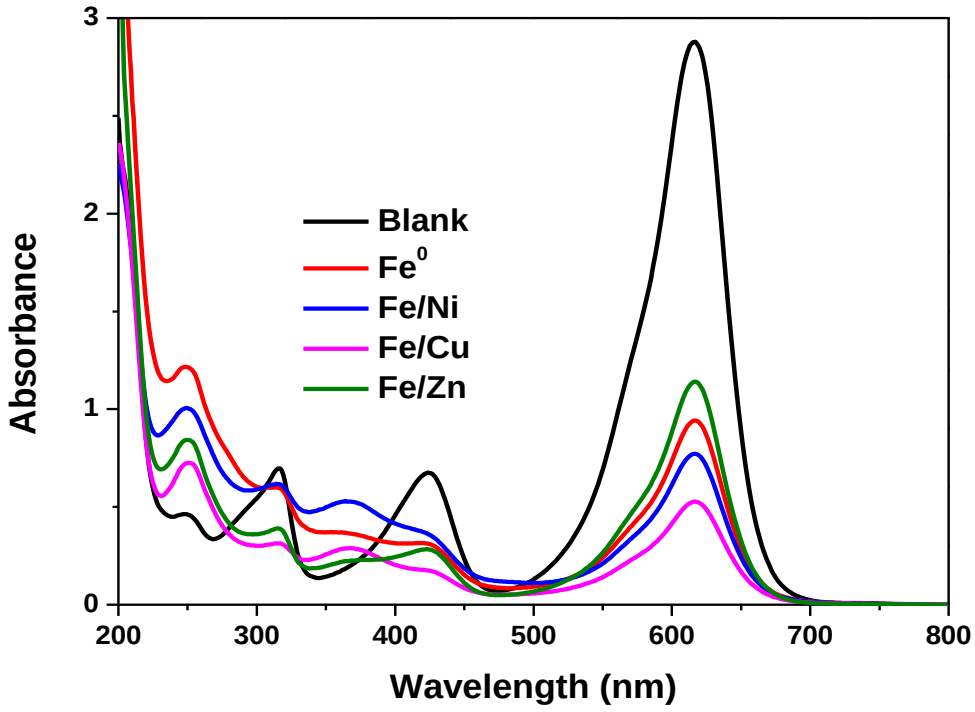

Figure 3.11 *UV-visible spectra of MG dye after treating with Fe^0, Fe/Ni, Fe/Cu and Fe/Zn nanoparticles*

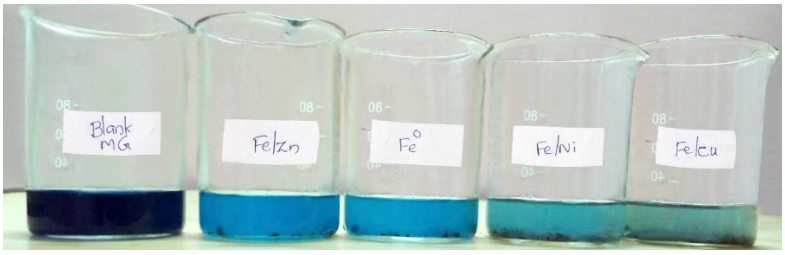

Figure 3.12 *Photographs of MG dye removal using Fe^0, Fe/Ni, Fe/Cu and Fe/Zn nanoparticles*

Effect of nanoparticle dosage

Effect of nanoparticle dosage on MG dye removal has been studied using Fe^0, Fe/Ni, Fe/Zn and Fe/Cu nanoparticles in different nanoparticle dosages varying from 0.25 g/L to 1 g/L by keeping MG concentration (50 mg/L) and contact time (15 min) as constant. As shown in figure 3.13a, the highest removal efficiency was exhibited by Fe/Cu bimetallic nanoparticles, followed by Fe/Ni, Fe^0 and Fe/Zn nanoparticles. At the dosage of 0.5 g/L, 73 %, 65 %, 59 % and 53 % of dye molecules were decolourised using Fe/Cu, Fe/Ni, Fe^0 and Fe/Zn nanoparticles respectively. With the increase in nanoparticle dosage, the availability of active reactive sites and total surface area increase, it was eventually leading to more decolourisation of dye molecules. All bimetallic nanoparticles showed the same trend. However, in the dosage of 1 g/L, there will be a decrease in the rate of dye decolourisation. It implies that at higher nanoparticle dosage, aggregation and overlapping of nanoparticles reduced the active surface area and eventually leads a decline in the decolourisation of dye molecules[36].

Effect of the initial concentration of MG

The effect of the initial concentration of MG in the dye decolourisation has been studied in 10-50 mg/L dye solutions by keeping nanoparticle dosage (0.5 g/L) and contact time (15 min) constant. As shown in figure 3.13b, 10 mg/L dye solutions were removed more efficiently than 50 mg/L dye solutions. The Fe/Cu, Fe/Ni, Fe^0 and Fe/Zn nanoparticles show 82 %, 69 %, 68 % and 59 % of removal efficiency respectively for MG dye solution. The remarkable decrease in dye removal efficiency with concentration is mainly attributed to the increased electrostatic repulsive interaction between the adsorbed cationic molecules with concentration.

Effect of contact time

The removal efficiency of nanoparticles was greatly influenced by the interaction time between nanoparticles and dye molecules. In this study, the effect of contact time on dye removal has been studied (figure 3.13c) by varying the contact time (5- 30 min) between the nanoparticles and dye molecules by keeping all other parameters constant. The result shows that the nanoparticles removal efficiency increases with increasing contact time upto a specific time and after that the percentage removal efficiency tends to an equilibrium point. Initially, the number of surface active sites was more for adsorption and degradation, leading to the rapid decolourisation of dye molecules. After some time, the

surface passive layer was formed due to iron corrosion and the surface adsorptive sites were filled with dye molecules. This leads to a decrease in the decolourisation rate of dye molecules[37].

Effect of pH

The effect of pH on dye removal has been studied and shown in figure 3.13d. The results envisage that acidic pH was preferred by the iron-based nanoparticles for better removal efficiency. There is not much significant difference in removal efficiency from neutral to alkaline pH. Fe/Cu bimetallic nanoparticles show the highest removal efficiency in acidic pH. The removal efficiency of 58 %, 68 %, 74 % and 78 % were shown by Fe/Zn, Fe^0, Fe/Ni and Fe/Cu nanoparticles respectively. At acidic pH, the electron transfer and production of reactive species were enhanced causing the better degradation of MG dye molecules. However, there may be a chance for a decrease in the adsorption of dye molecules due to the electrostatic repulsion between the positively charged surface of iron nanoparticles and cationic MG dye molecules. When the pH of the solution increases, there will be a decrease in electrostatic repulsion, promoting the adsorption of the dye molecules. Nevertheless, the formation of the surface passive layer in the surface of the iron nanoparticles reduces the electron transfer from the Fe^0 core in basic pH. In this case, the high removal efficiency at acidic pH inferred that degradation is the major mechanism for dye removal compared to adsorption[36–38].

Effect of second metal deposition on Fe^0

The percentage of second metal deposition in the Fe^0 has a vital role in removing dye molecules. The effect of the second metal dosage on dye removal has been studied (figure 3.13e) by changing the second metal dosage from 5 % to 15 % by keeping all other parameters such as initial dye concentration (50 mg/L), nanoparticle dosage (0.5 g/L) and contact time (15 min) constant. The results show that 10 % bimetal loading shows better removal efficiency than 5 % and 15 % bimetal loading. This shows that 5 % bimetal loading was not sufficient to improve the property of Fe nanoparticles. When the second metal % increases, more electron transfer and formation of reactive oxygen species occur, leading to more removal efficiency. However, the excess quantity of the second metal led to increased nanoparticle agglomeration and decreased the interaction between iron nanoparticles and dye molecules. It will eventually cause a decrease in the removal efficiency[39].

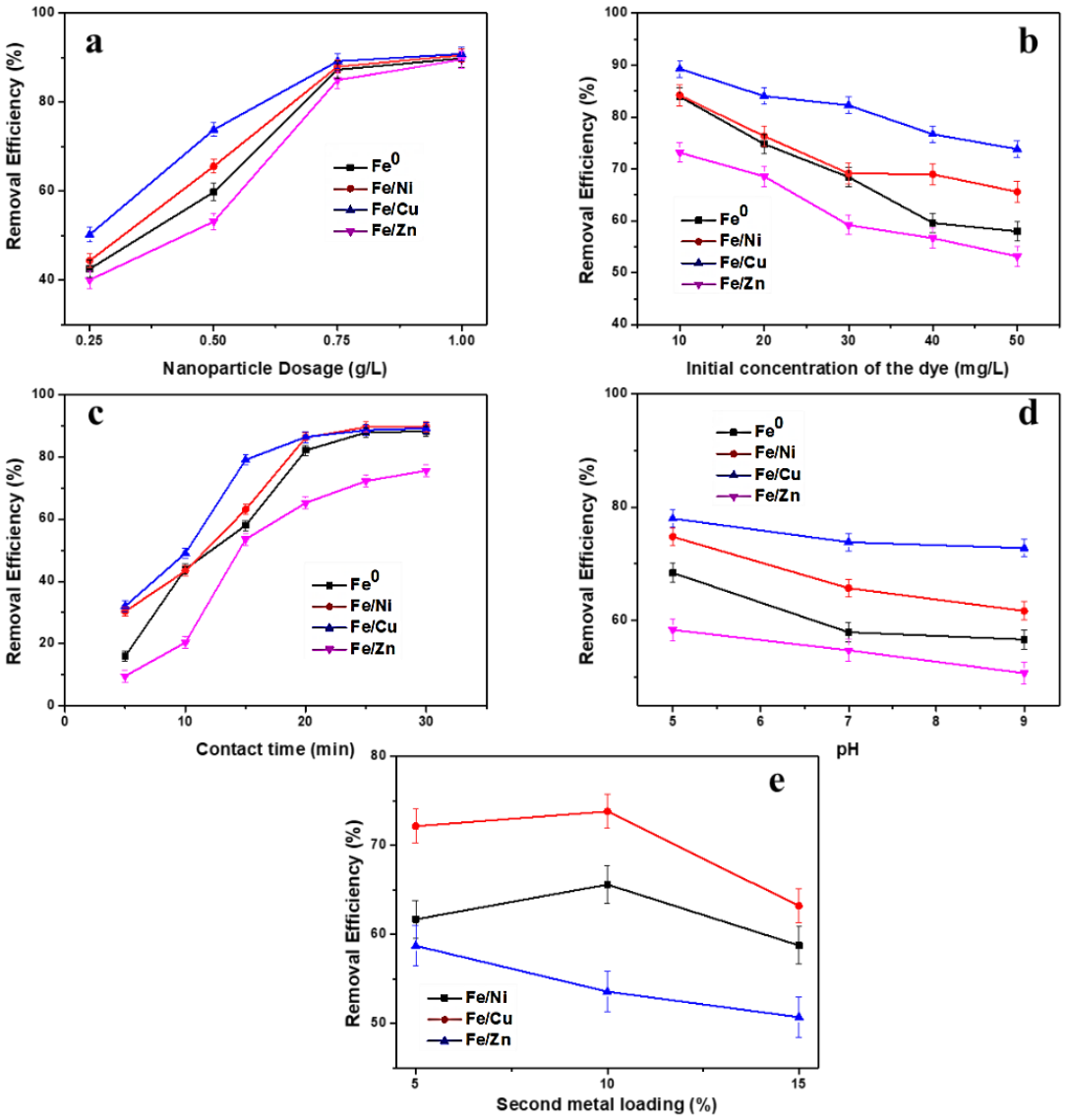

Figure 3.13 *(a) Effect of nanoparticle dosage (b) Effect of initial concentration of MG (c) Effect of contact time (d) Effect of pH (e) Effect of second metal loading in MG dye removal using Fe^0, Fe/Ni, Fe/Cu and Fe/Zn nanoparticles*

GC-MS/MS analysis

To determine the volatile degradation product of MG, GC-MS/MS study has been performed after complete decolourisation of dye solution using Fe^0 nanoparticles. GC-MS/MS analysis identified two possible degradation products using the NIST library. Mass spectra of the identified products are shown in figure 3.14(a&b). One possible intermediate eluted at 7.83 min was identified as cyclohexa-2,5-diene-1,4-dione (MW 108) and another degradation product eluted at 19.90 min was confirmed as diphenylmethanone (MW 182). The two degradation products indicated by GC-MS/MS

could result from the destruction of the entire conjugated chromophore structure of MG. The area covered by diphenylmethanone was 4.30, implying that it was the major degradation product. The formation of these stable compounds results from the interaction of reactive oxygen species and other active species with dye molecules.

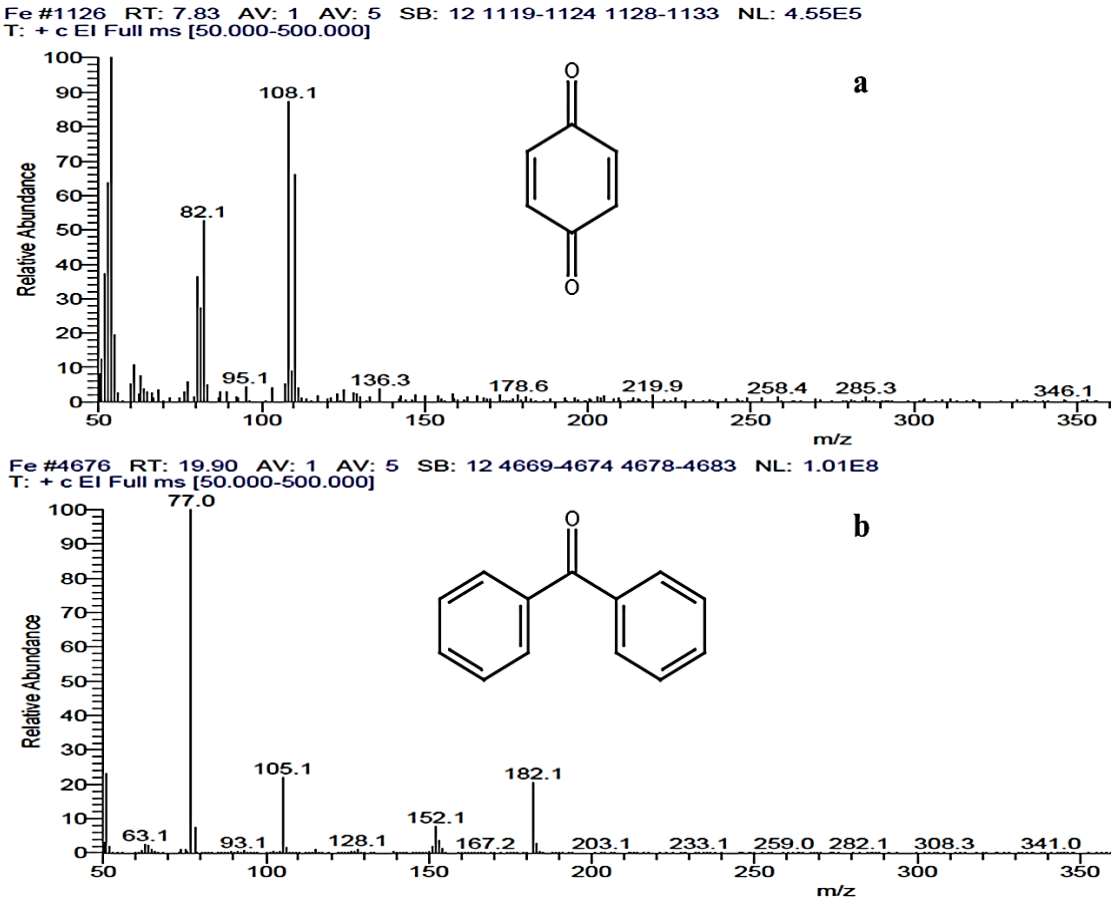

Figure 3.14 *Mass spectra of MG degradation products identified by GC-MS/MS analysis a) cyclohexa-2,5-diene-1,4-dione and b) diphenylmethanone*.

LC-MS/MS analysis

In order to provide the supportive information for the proposed degradation mechanism of MG dye molecules, LC-MS/MS study has been carried out in the solution of MG. Figure 3.15 shows the MG solution's LC-MS/MS chromatogram after being treated with Fe^0 nanoparticles. MG has been detected in retention time (Rt) 69.79 min with m/z 330. The degradation products identified and their m/z values and Rt are listed in table 3.2. All the identified compounds did not show an apparent peak in the LC-MS/MS chromatogram but were detected by mass spectrometry.

Compound	IUPAC name	Rt (min)	m/z
MG	4-[4-(dimethylamino)phenyl]-phenyl-methylene]cyclohexa-2,5-dien-1-ylidene]-dimethyl-ammonium	69.79	330.3359
MG-CH_2	dimethyl-[4-[[4-(methylamino)phenyl]-phenyl-methylene]cyclohexa-2,5-dien-1-ylidene]azanium	58.6	316.2841
MG-$2CH_2$	dimethyl-[4-[[4-(methylamino)phenyl]-phenyl-methylene]cyclohexa-2,5-dien-1-ylidene]ammonium	65.28	302.3052
MG-$3CH_2$	[4-[(4-aminophenyl)-phenyl-methylene]cyclohexa-2,5-dien-1-ylidene]-methylazanium	61.74	288.2888
MG-$4CH_2$	[[4-[(4-aminophenyl)-phenyl-methylene]cyclohexa-2,5-dien-1-ylidene]azanium	50.74	274.2735
MG-$2CH_2$-NH_2	4-(dimethylamino)tritylradical	56.0	287.1552
LMG	4-[[4-(dimethylamino)phenyl]-phenyl-methyl]-N,N-dimethyl-aniline	46.63	331.2081
LMG-CH_2	4-[[4-(dimethylamino)phenyl]-phenyl-methyl]-N-methyl-aniline	60.1	317.1720
LMG-$3CH_2$	4-[[4-(methylamino)phenyl]-phenylmethyl]aniline	33.74	289.1259
LMG-$4CH_2$-NH_2	4-benzhydrylaniline	57.95	260.2579
LMG-$4CH_2$-$2NH_2$	benzhydrylbenzene	60.74	245.0781
LMG+OH	4-[bis[4-(dimethylamino)phenyl]methyl]phenol	37.31	347.1304

LMG+2OH	5-[bis[4-(dimethylamino)phenyl]methyl]benzene-1,3-diol	68.90	363.3090
LMG+OH-CH_2-CH_3	N-[4-[[4-(dimethylamino)phenyl]-phenylmethyl]phenyl]hydroxylamine	69.1	319.2836
LMG+OH-4CH_2	4-[bis(4-aminophenyl)methyl]phenol	60.4	290.2696
DLBP	[4-(dimethylamino)phenyl]-phenylmethanone	62.6	226.1229
DLBP -CH_2	[4-(methylamino)phenyl]-phenylmethanone	60.05	212.1069
DLBP +OH	[4-(dimethylamino)phenyl]-(4-hydroxyphenyl)methanone	65.30	242.2841
DLBP +OH -CH_2	[3-hydroxy-4-(methylamino)phenyl]-phenylmethanone	63.46	228.2679
DLBP +OH -2CH_2	(4-aminophenyl)-(4-hydroxyphenyl)methanone	58.3	214.2528
DLBP +2OH -2CH_2	(4-aminophenyl)-(2,4-dihydroxyphenyl)methanone	52.3	230.2467
$C_8H_{11}N$	N,N-dimethylaniline	70.07	122.0965
$C_9H_{11}O_2N$	4-(dimethylamino)benzoic acid	51.8	166.0866

Table 3.2 *Products identified by LC-MS/MS*

Compared to GC-MS/MS analysis, more degradation products were identified by LC-MS/MS analysis since several volatile degradation products are too low to be eluted under the gas chromatographic conditions used. Mass spectra of some degradation products are shown in figure 3.16.

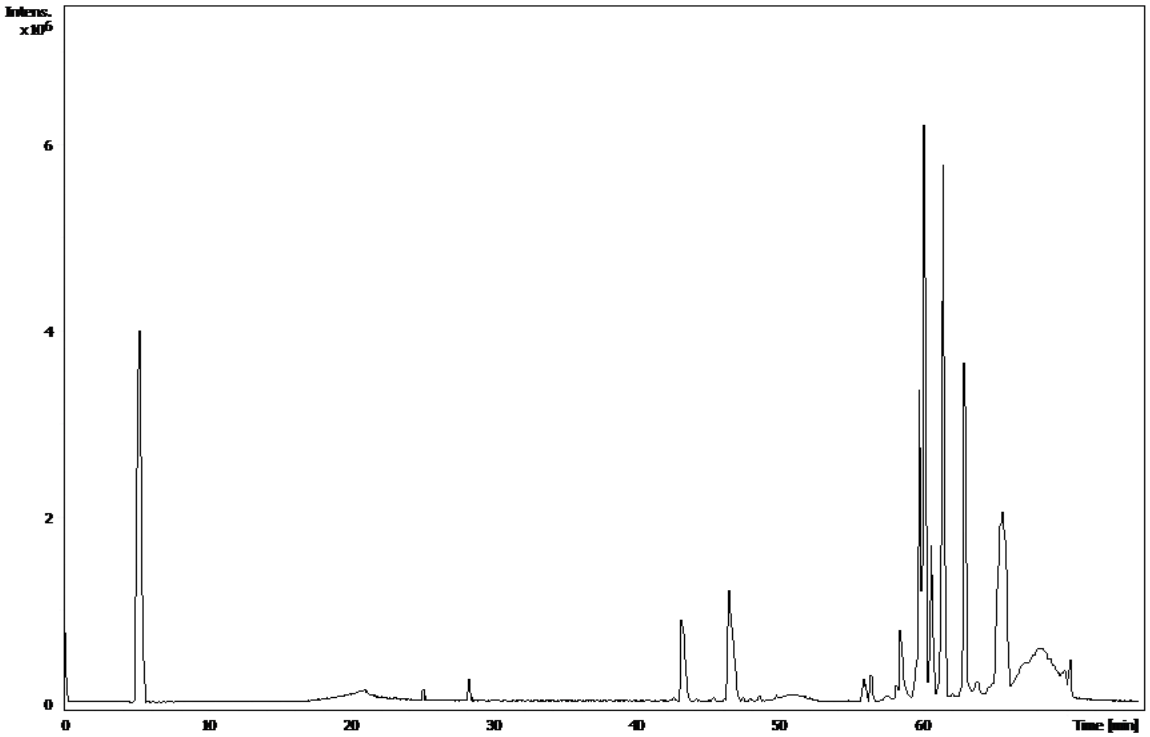

Figure 3.15 *LC-MS/MS of MG degradation products after treating with Fe^0 nanoparticles*

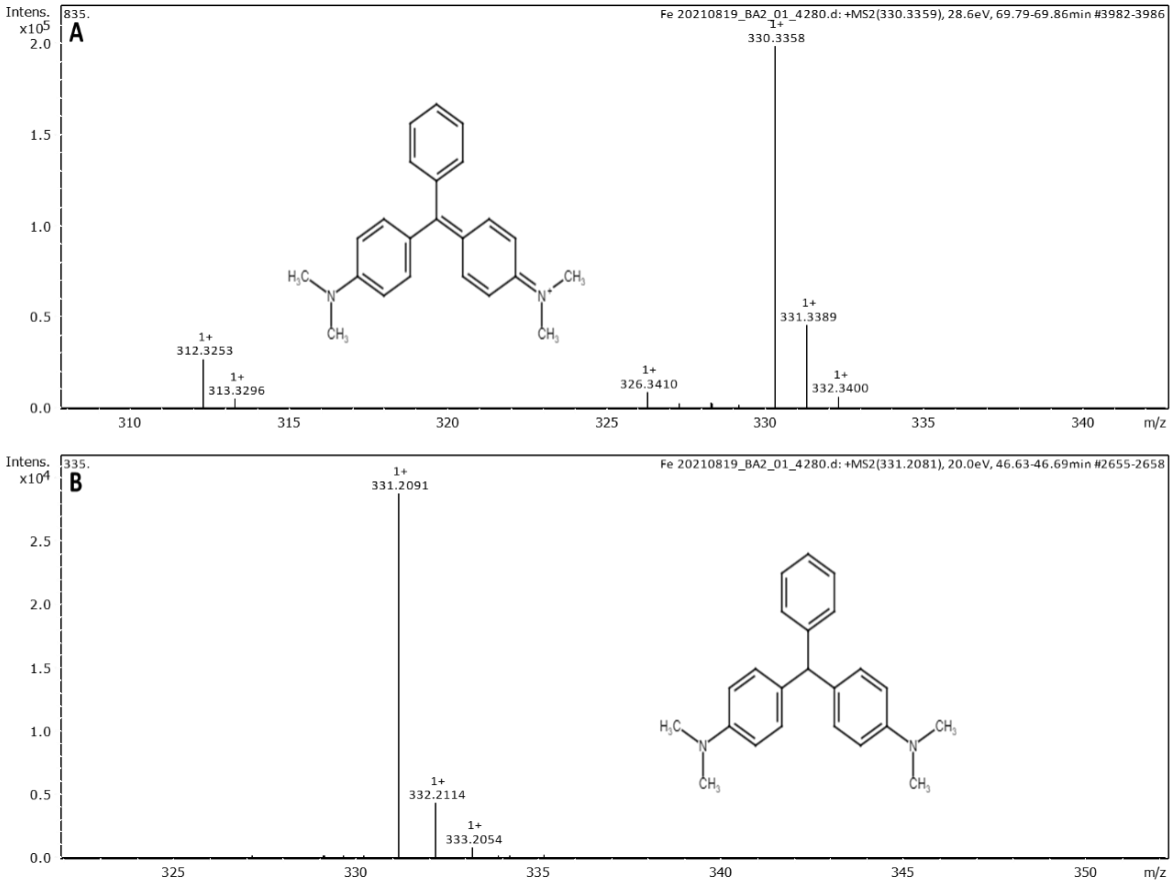

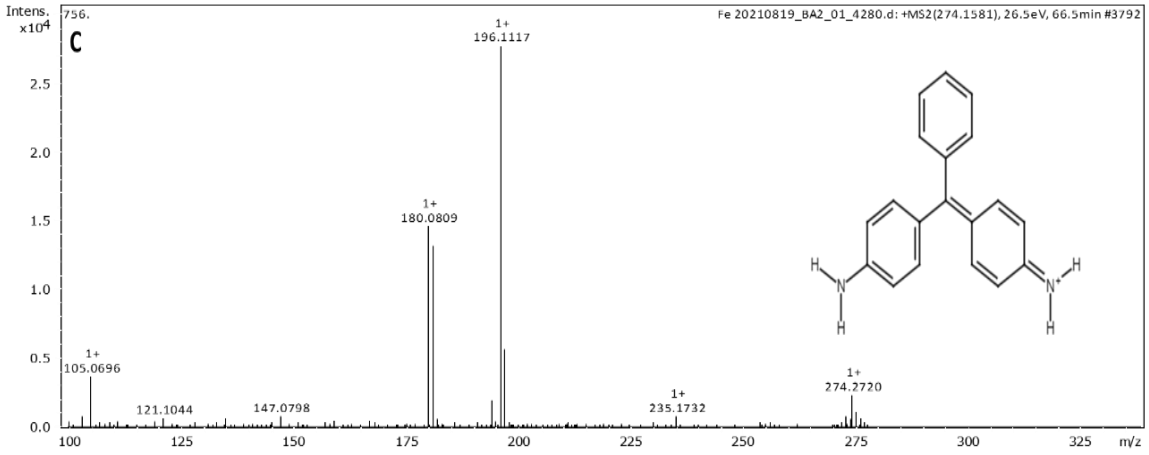
Intens.
x10^4
C
Fe 20210819_BA2_01_4280.d: +MS2(274.1581), 26.5eV, 66.5min #3792
1+ 196.1117
1+ 180.0809
1+ 105.0696
121.1044
147.0798
1+ 235.1732
1+ 274.2720
m/z

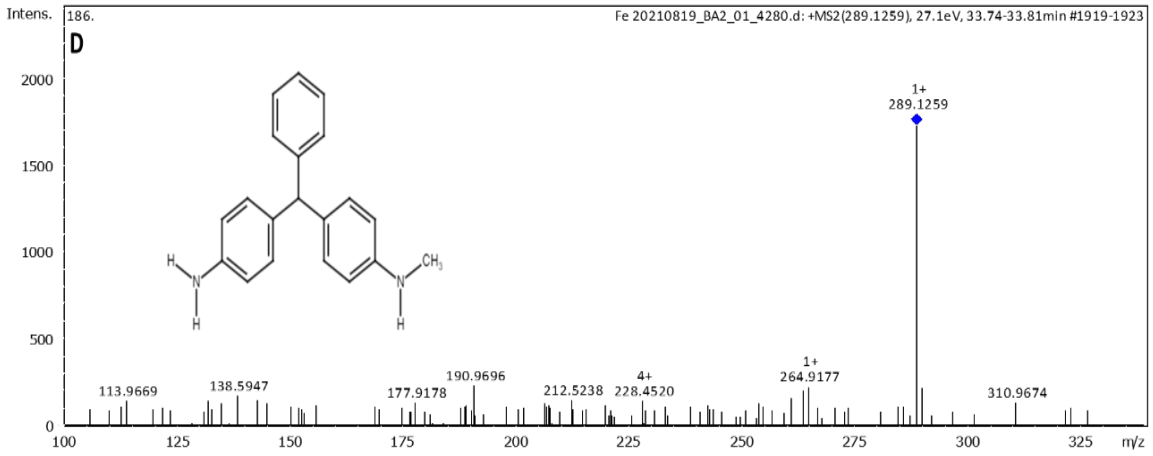
Intens.
D
Fe 20210819_BA2_01_4280.d: +MS2(289.1259), 27.1eV, 33.74-33.81min #1919-1923
1+ 289.1259
113.9669
138.5947
177.9178
190.9696
212.5238
4+ 228.4520
1+ 264.9177
310.9674
m/z

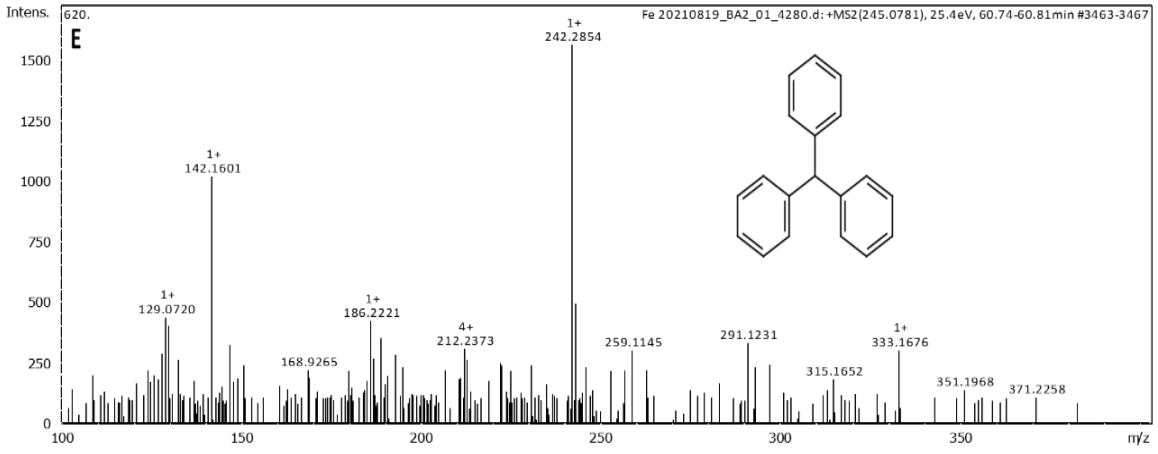
Intens.
E
Fe 20210819_BA2_01_4280.d: +MS2(245.0781), 25.4eV, 60.74-60.81min #3463-3467
1+ 242.2854
1+ 142.1601
1+ 129.0720
1+ 186.2221
4+ 212.2373
168.9265
259.1145
291.1231
1+ 333.1676
315.1652
351.1968
371.2258
m/z

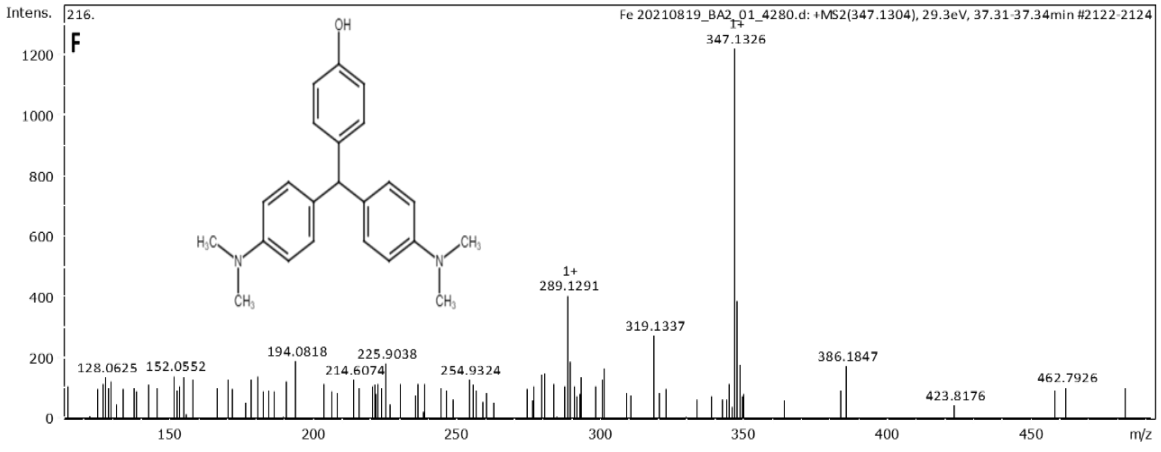
Intens.
F
Fe 20210819_BA2_01_4280.d: +MS2(347.1304), 29.3eV, 37.31-37.34min #2122-2124
1+ 347.1326
1+ 289.1291
319.1337
194.0818
225.9038
214.6074
254.9324
128.0625
152.0552
386.1847
423.8176
462.7926
m/z

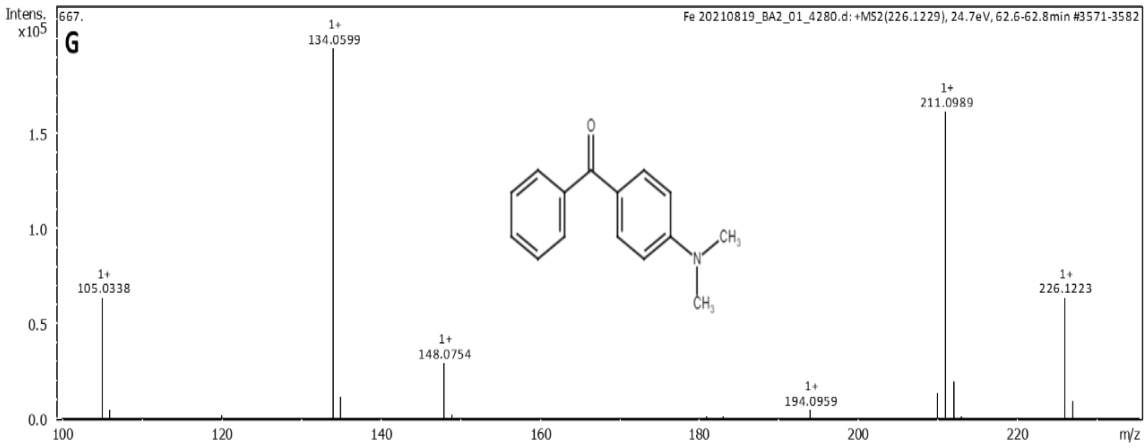
Intens.
x10^5
667.
G
Fe 20210819_BA2_01_4280.d: +MS2(226.1229), 24.7eV, 62.6-62.8min #3571-3582
1+
134.0599
1+
211.0989
1+
105.0338
1+
226.1223
1+
148.0754
1+
194.0959
O
N
CH3
CH3
0.0
0.5
1.0
1.5
100
120
140
160
180
200
220
m/z

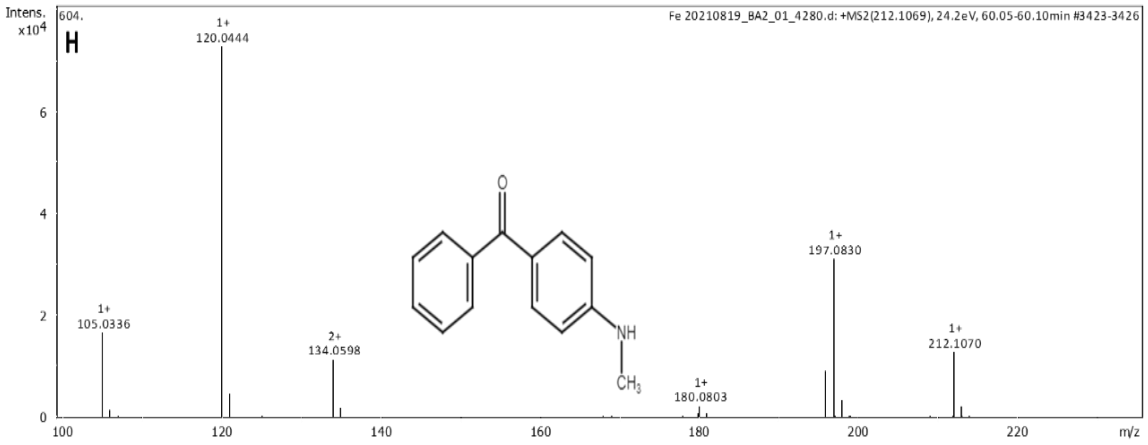
Intens.
x10^4
604.
H
Fe 20210819_BA2_01_4280.d: +MS2(212.1069), 24.2eV, 60.05-60.10min #3423-3426
1+
120.0444
1+
197.0830
1+
105.0336
2+
134.0598
1+
212.1070
1+
180.0803
O
NH
CH3
0
2
4
6
100
120
140
160
180
200
220
m/z

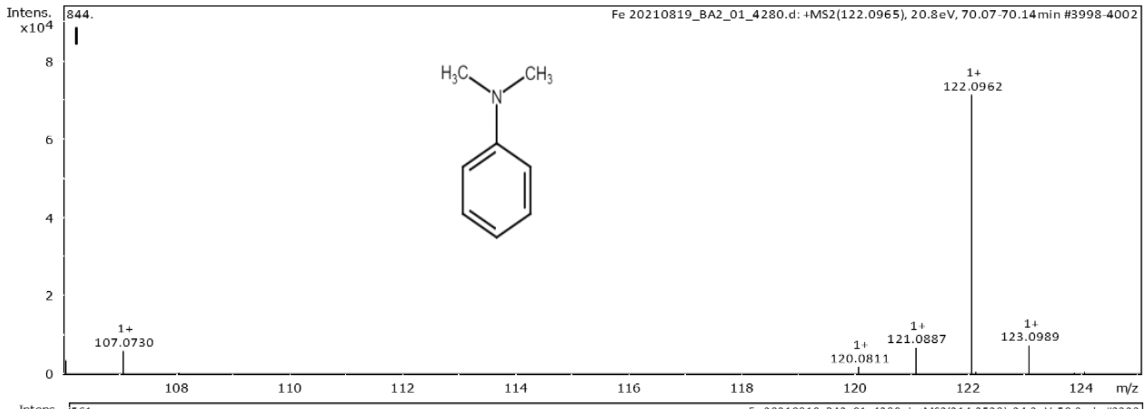
Intens.
x10^4
844.
I
Fe 20210819_BA2_01_4280.d: +MS2(122.0965), 20.8eV, 70.07-70.14min #3998-4002
H3C
N
CH3
1+
122.0962
1+
107.0730
1+
120.0811
1+
121.0887
1+
123.0989
0
2
4
6
8
108
110
112
114
116
118
120
122
124
m/z

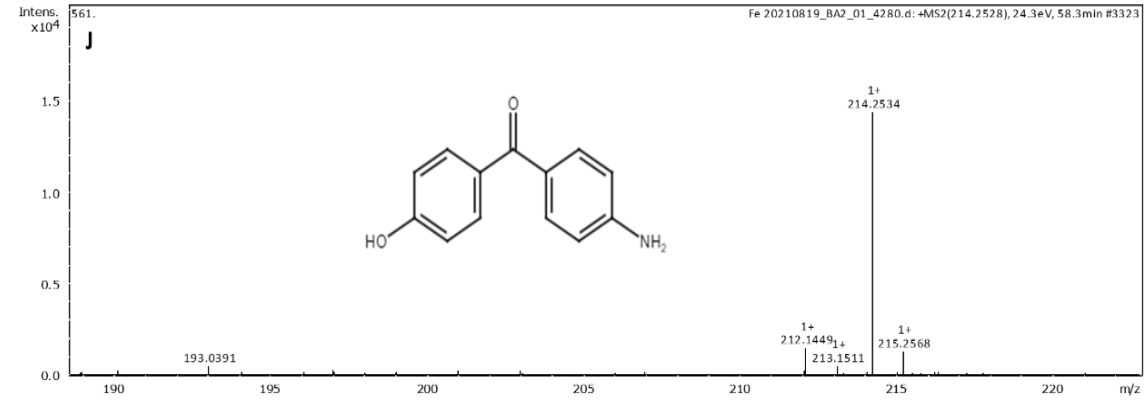
Intens.
x10^4
561.
J
Fe 20210819_BA2_01_4280.d: +MS2(214.2528), 24.3eV, 58.3min #3323
1+
214.2534
O
HO
NH2
1+
212.1449
1+
213.1511
1+
215.2568
193.0391
0.0
0.5
1.0
1.5
190
195
200
205
210
215
220
m/z

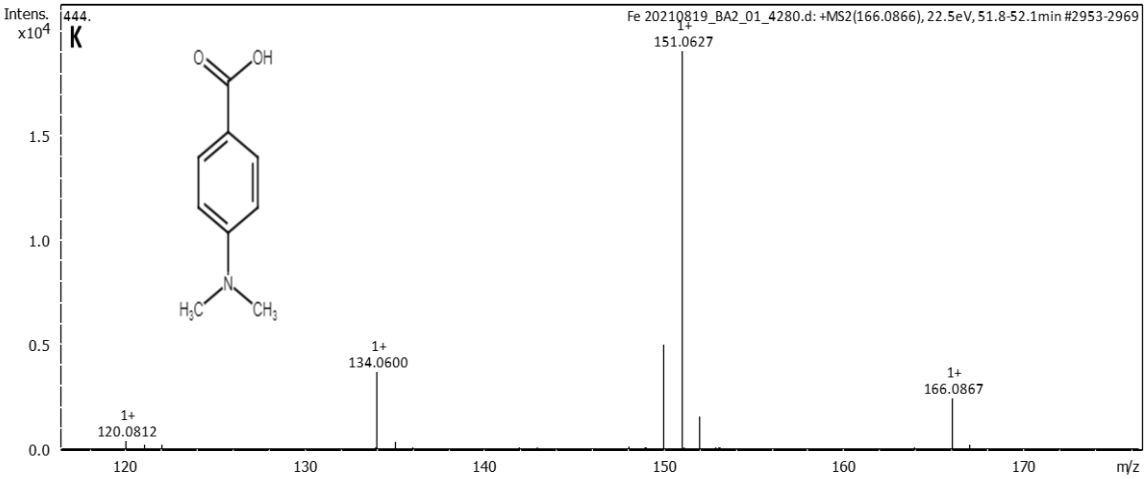

Figure 3.16 *Mass spectra of some MG degradation products identified by LC-MS/MS analysis. (A) [4-[[4-(dimethylamino)phenyl]-phenylmethylidene]cyclohexa-2,5-dien-1-ylidene]-dimethylazanium; (B) 4-[[4-(dimethylamino)phenyl]-phenylmethyl]-N,N-dimethylaniline; (C) [4-[(4-aminophenyl)-phenylmethylidene]cyclohexa-2,5-dien-1-ylidene] azanium; (D) 4-[[4-(methylamino)phenyl]-phenylmethyl]aniline; (E) benzhydrylbenzene ; (F) 4-[bis[4-(dimethylamino)phenyl]methyl]phenol; (G) [4-(dimethylamino)phenyl]-phenylmethanone; (H) [4-(methylamino)phenyl]-phenylmethanone; (I)* N,N-dimethyl aniline*;(J)* (4-aminophenyl)-(4-hydroxyphenyl)methanone*;(K) 4-(dimethylamino)benzoic acid*

Proposed mechanism for the degradation of MG using Fe nanoparticles

The degradation of MG involves both reductive and oxidative pathways along with the adsorption of the dye molecules. The reductive degradation of MG depends on the Fe^0 content and H^+ in the solution. During the reductive pathway, the MG molecules may adsorb onto the iron surface and degradation occurs through direct electron transfer or adsorbed H*. The two adsorbed atomic hydrogen can combine to form H_2[40]. These reactions in the reductive pathway are shown in equations 3.8-3.11.

$$Fe^0 \rightarrow Fe^{2+} + 2e^- \tag{3.8}$$

$$2Fe^0 + 2H^+ + 2e^- \rightarrow 2Fe - H^* \rightarrow 2Fe + H_2 \tag{3.9}$$

$$Dye + e^- \rightarrow Degradation\ products \tag{3.10}$$

$$Dye + 2Fe - H^* \rightarrow Degradation\ products \tag{3.11}$$

During the reductive degradation of MG dye, the MG was first reduced into leuco MG. After the initial stage of the degradation process, the degradation mechanism prevailed by oxidative pathway since the MG dye removal experiment did not take place in anaerobic

system. In the presence of dissolved oxygen, the iron oxide layer formed quickly and decreased the probability of reductive degradation. The addition of second metal (Ni, Cu) changes the faith of Fe^0 nanoparticles upto an extent. Deposition with a second metal improves iron corrosion and hydrogen generation and prevents the blocking of the iron surface through the formation of oxide film[41]. The reductive removal of MG with bimetallic nanoparticles were shown in equation 3.12-3.14. The second metal (Ni or Cu) loses the electrons while reacting with the dye molecule. The formed nickel or copper ion was galvanically protected by electrons released from Fe/Fe^{2+} and Fe^{2+}/Fe^{3+} redox reactions and turned into metallic Ni or Cu again. This process will continue until there is an electronic bridge between the two metals. Along with the direct electron transfer, the hydride formation with deposited metal would also play an essential role in reductive dye degradation in bimetallic nanoparticles. Nickel hydride or copper hydride was formed by reacting with the atomic hydrogen. These hydride formations reductively degrade the MG molecules (as shown in equation 3.15-3.18) and during this time, a new hydride free surface formed in iron-based bimetals[41,42].

$$Fe^0 \rightarrow Fe^{2+} + 2e^- \quad (3.12)$$

$$Ni^{2+}/\ Cu^{2+} + 2e^- \rightarrow Ni^0/Cu^0 \quad (3.13)$$

$$Ni^0/Cu^0 + MG + H_2O \rightarrow Ni^{2+}/\ Cu^{2+} + MG_{reduced} + OH^- \quad (3.14)$$

$$2H_2O + 2e^- \rightarrow 2H^* + 2OH^- \quad (3.15)$$

$$Ni + H^* \rightarrow Ni - H^* \quad (3.16)$$

$$Cu + H^* \rightarrow Cu - H^* \quad (3.17)$$

$$Ni - H^*/\ Cu - H^* + MG \rightarrow Ni/Cu + MG\ degradation\ products \quad (3.18)$$

The oxidative removal of MG dye prevailed over time than reductive removal conditions. The iron nanoparticle acted as a heterogeneous Fenton-like catalysts since the iron nanoparticles react with dissolved oxygen in water and form reactive oxygen species like hydrogen peroxide, hydroxyl radical etc.[43–45] as shown in equations 3.19-3.23.

$$O_2 + 2e^- + 2H^+ \rightarrow 2\ \cdot OH \quad (3.19)$$

$$2Fe^0 + O_2 + 2H_2O \rightarrow 2Fe^{2+} + 2H_2O_2 \quad (3.20)$$

$$Fe^{2+} + H_2O_2 \rightarrow Fe^{3+} + \cdot OH + OH^- \quad (3.21)$$

$$Fe^{3+} + H_2O_2 \rightarrow Fe^{2+} + \cdot OOH + H^+ \quad (3.22)$$

$$Fe^{3+} + \cdot OOH \rightarrow Fe^{2+} + O_2 + H^+ \quad (3.23)$$

Hydroxyl radical formed by the reaction was reacted with the MG dye molecule and degraded them into smaller fragments. Bimetallic composition in the iron-based nanoparticles will improve the formation of hydroxyl radicals. For example, the formation of hydroxyl radical by Fe/Cu bimetallic nanoparticles[1] has been shown in equation 3.24.

$$Fe^{2+} + Cu^{2+} + 3H_2O_2 \rightarrow 3\ \cdot OH + HO_2 \cdot + H_2O + Fe^{3+} + Cu^{2+} \quad (3.24)$$

The MG and its degradation products are adsorbed onto the surface of Fe^0 and iron oxides as shown in equations 3.25 and 3.26.

$$Fe^0 + MG \rightarrow Fe^0 - MG \quad (3.25)$$

$$Fe_xO_y/FeOOH + MG\ degradation\ products \rightarrow Fe_xO_y/FeOOH - MG\ degradation\ products \quad (3.26)$$

The degradation pathway of MG by Fe^0 nanoparticles is shown in scheme 3.1. A few undetected degradation products are also depicted in scheme 3.1, including b2, b4, c4, d2, d8, e1, e2 and e4. Even though these degradation products were not detected in GC-MS/MS and LC-MS/MS analysis, the presence of some other compounds inferred the existence of these compounds.

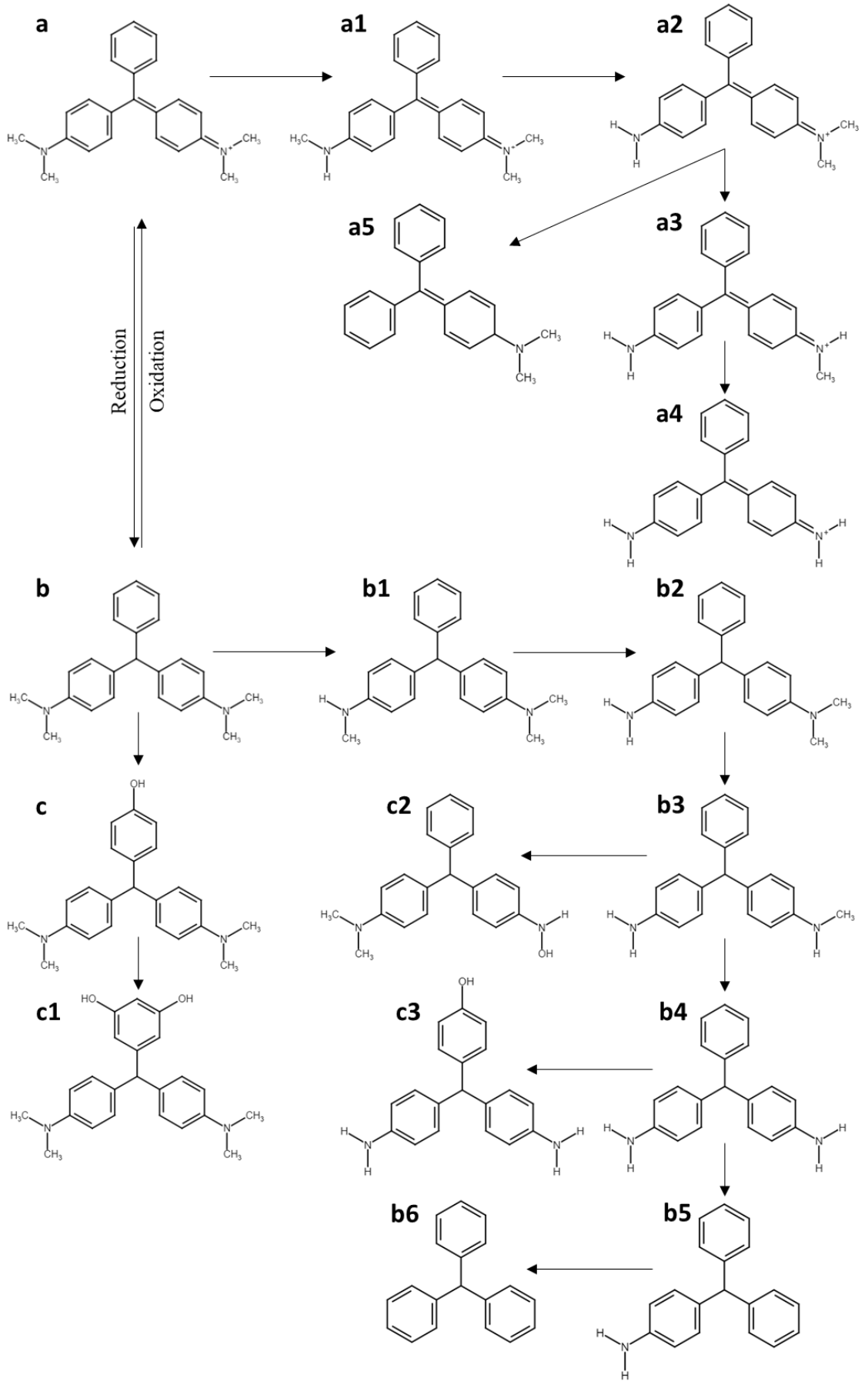
a
a1
a2
a3
a4
a5
Reduction
Oxidation
b
b1
b2
b3
b4
b5
b6
c
c1
c2
c3

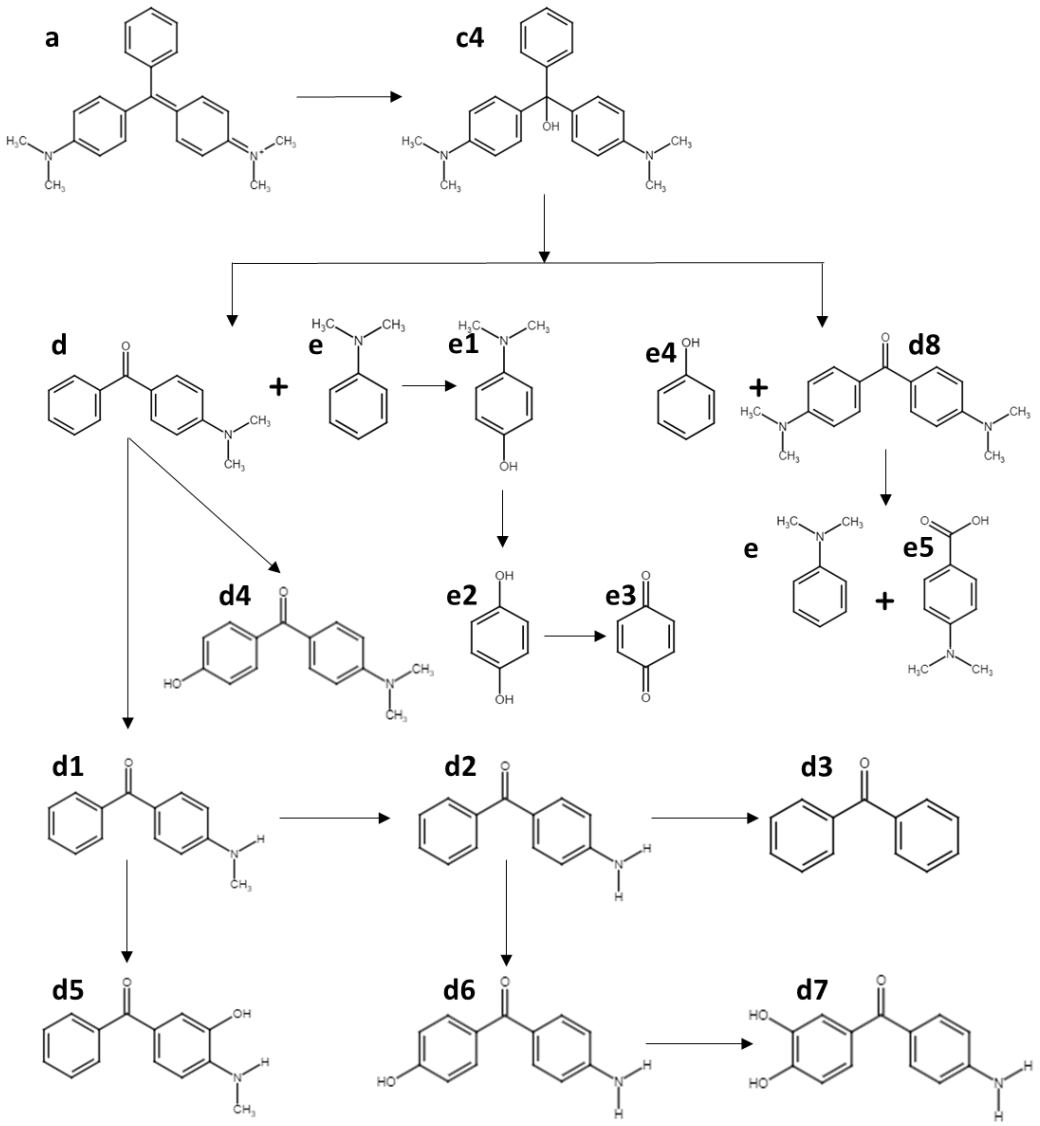

Scheme 3.1 *Degradation pathways of MG using Fe^0 nanoparticle*

MG degradation pathway shows that the attack by hydroxyl radical leads to the N-demethylation and deamination of MG and MG degradation products. N-demethylation has gradually occurred until the total elimination of the 4 methyl groups and deamination removes the amino group in the MG[18]. In the scheme, a1-a4, b1-b6 and d1-d3 represent the N-demethylation and deamination of MG and its degradation products. The next set of reactions that occurred in MG is hydroxyl addition reactions. The addition of hydroxyl radical happened in MG degradation products due to the non-selectivity of hydroxyl radical[46]. The products c-c4 and d4-d7 represent the results of hydroxyl addition reactions in MG and MG degradation products. The hydroxyl radical attacked the central

carbon leading to the destruction of the conjugated structure. The c4 so formed gets degraded in two ways, (1) N,N-dimethylaniline (e) and [4-(dimethylamino)phenyl]-phenylmethanone (d), and (2) phenol (e4) and bis[4-(dimethylamino)phenyl]methanone (d8)[18,47]. N-demethylation, deamination and hydroxyl addition reactions occurred in N,N-dimethylaniline leading to hydroquinone formation. These formed hydroquinone molecules were suddenly transferred into cyclohexa-2,5-diene-1,4-dione in the presence of H_2O_2[48–50]. The bis[4-(dimethylamino)phenyl]methanone is further degraded into N,N-dimethylaniline and 4-(dimethylamino)benzoic acid (e5) by reacting with hydroxyl radical[18]. There will be a chance for further degradation and mineralisation of MG degraded products, but not detected by LC-MS/MS since below m/z 100 was not examined in this study.

3.4 Conclusions

In this study, zero valent iron nanoparticles and bimetallic iron-based nanoparticles were prepared through the liquid-phase reduction method using $NaBH_4$ as the reducing agent. The characterisation of the prepared nanoparticles has been done using XRD, HRTEM and EDAX and confirmed the formation of Fe^0, Fe/Ni, Fe/Zn and Fe/Cu nanoparticles. The reactivity of prepared nanoparticles was studied for Cr(VI) and dye removal and found that Fe/Cu and Fe/Ni bimetallic nanoparticles were more efficient than Fe^0 and Fe/Zn nanoparticles. The better efficiency of Fe/Cu and Fe/Ni bimetallic nanoparticles was due to their better direct electron transfer, hydride formation and formation of reactive oxygen species. The effect of various parameters such as initial concentration of the dye, nanoparticle dosage, initial pH of the solution, contact time and deposition of second metal has been examined in this study. Both MG dye and Cr(VI) removal preferred acidic pH and a second metal deposition of 10 %. Iron-based nanoparticles effectively removed the triphenylmethane dyes compared to azo and thiazine dyes. EDAX confirmed the reduction of Cr(VI) by prepared nanoparticles and the degradation of MG dye molecules was confirmed by GC-MS/MS and LC-MS/MS techniques. Thus, Fe/Ni and Fe/Cu bimetallic nanoparticles can be used as a cost-effective and practical material for Cr(VI) and MG dye removal.

3.5 References

[1] J. Scaria, P. V. Nidheesh, M.S. Kumar, Synthesis and applications of various bimetallic nanomaterials in water and wastewater treatment, J. Environ. Manage. 259 (2020) 110011. https://doi.org/10.1016/j.jenvman.2019.110011.

[2] D. O'Carroll, B. Sleep, M. Krol, H. Boparai, C. Kocur, Nanoscale zero valent iron and bimetallic particles for contaminated site remediation, Adv. Water Resour. 51 (2013) 104–122. https://doi.org/10.1016/j.advwatres.2012.02.005.

[3] N. Toshima, T. Yonezawa, Bimetallic nanoparticles - Novel materials for chemical and physical applications, New J. Chem. 22 (1998) 1179–1201. https://doi.org/10.1039/a805753b.

[4] T. Shubair, O. Eljamal, A.M.E. Khalil, A. Tahara, N. Matsunaga, Novel application of nanoscale zero valent iron and bimetallic nano-Fe/Cu particles for the treatment of cesium contaminated water, J. Environ. Chem. Eng. 6 (2018) 4253–4264. https://doi.org/10.1016/j.jece.2018.06.015.

[5] R. Wang, T. Tang, K. Huang, M. Zou, X. Tao, H. Yin, Z. Lin, Z. Dang, G. Lu, Debromination of polybrominated biphenyls (PBBs) by zero valent metals and iron-based bimetallic particles: Mechanisms, pathways and predicting descriptor, Chem. Eng. J. 351 (2018) 773–781. https://doi.org/10.1016/j.cej.2018.06.149.

[6] R. Wang, G. Lu, H. Lin, K. Huang, T. Tang, X. Xue, X. Yang, H. Yin, Z. Dang, Relative roles of H-atom transfer and electron transfer in the debromination of polybrominated diphenyl ethers by palladized nanoscale zerovalent iron, Environ. Pollut. 222 (2017) 331–337. https://doi.org/10.1016/j.envpol.2016.12.030.

[7] R. Wang, T. Tang, G. Lu, Z. Zheng, K. Huang, H. Li, X. Tao, H. Yin, Z. Shi, Z. Lin, F. Wu, Z. Dang, Mechanisms and pathways of debromination of polybrominated diphenyl ethers (PBDEs) in various nano-zerovalent iron-based bimetallic systems, Sci. Total Environ. 661 (2019) 18–26. https://doi.org/10.1016/j.scitotenv.2019.01.166.

[8] Z. Xiong, B. Lai, P. Yang, Y. Zhou, J. Wang, S. Fang, Comparative study on the reactivity of Fe/Cu bimetallic particles and zero valent iron (ZVI) under different conditions of N2, air or without aeration, J. Hazard. Mater. (2015). https://doi.org/10.1016/j.jhazmat.2015.05.006.

[9] K.K. Onchoke, S.A. Sasu, Determination of Hexavalent Chromium (Cr(VI)) Concentrations via Ion Chromatography and UV-Vis Spectrophotometry in Samples Collected from Nacogdoches Wastewater Treatment Plant, East Texas (USA), Adv. Environ. Chem. 2016 (2016) 1–10. https://doi.org/10.1155/2016/3468635.

[10] J.O. Ighere, K. Honjoya, R.C. Chawla, Using Ferrous Ion for the Reductive Degradation of Hexavalent Chromium, Adv. Chem. Eng. Sci. 05 (2015) 15–22. https://doi.org/10.4236/aces.2015.51002.

[11] F. Liu, Y. Lu, H. Chen, Y. Liu, Removal of Cr from groundwater using zero- valence iron in the laboratory Removal of Cr 6 + from groundwater using zero- valence iron in the laboratory, Chem. Speciat. Bioavailab. 2299 (2015) 2–5. https://doi.org/10.3184/095422902782775290.

[12] R.A. Anderson, Chromium as an Essential Nutrient for Humans, Regul. Toxicol. Pharmacol. 41 (1997). https://doi.org/10.1006/rtph.1997.1136.

[13] M.I.N. Ahamed, S. Rajeshkumar, V. Ragul, S. Anand, K. Kaviyarasu, Chromium remediation and toxicity assessment of nano zerovalent iron against contaminated lake water sample (Puliyanthangal Lake, Tamilnadu, India), South African J. Chem. Eng. 25 (2018) 128–132. https://doi.org/10.1016/j.sajce.2018.04.004.

[14] F. Liu, Y. Lu, H. Chen, Y. Liu, Removal of Cr 6+ from groundwater using zero-valence iron in the laboratory, Chem. Speciat. Bioavailab. 14 (2002) 75–77. https://doi.org/10.3184/095422902782775290.

[15] H. Oliveira, Chromium as an Environmental Pollutant: Insights on Induced Plant Toxicity, J. Bot. 2012 (2012) 1–8. https://doi.org/10.1155/2012/375843.

[16] A. Arunarani, P. Chandran, B. V. Ranganathan, N.S. Vasanthi, S. Sudheer Khan, Bioremoval of Basic Violet 3 and Acid Blue 93 by Pseudomonas putida and its adsorption isotherms and kinetics, Colloids Surfaces B Biointerfaces. 102 (2013) 379–384. https://doi.org/10.1016/j.colsurfb.2012.08.049.

[17] K.Z. Xu, H. Ma, Y.J. Wang, Y.J. Cai, X.R. Liao, Z.B. Guan, Extracellular expression of mutant CotA-laccase SF in Escherichia coli and its degradation of malachite green, Ecotoxicol. Environ. Saf. 193 (2020) 110335. https://doi.org/10.1016/j.ecoenv.2020.110335.

[18] L.N. Du, M. Zhao, G. Li, F.C. Xu, W.H. Chen, Y.H. Zhao, Biodegradation of malachite green by Micrococcus sp. strain BD15: Biodegradation pathway and enzyme analysis, Int. Biodeterior. Biodegrad. 78 (2013) 108–116. https://doi.org/10.1016/j.ibiod.2012.12.011.

[19] T. Bhagavathi Pushpa, J. Vijayaraghavan, S.J. Sardhar Basha, V. Sekaran, K. Vijayaraghavan, J. Jegan, Investigation on removal of malachite green using EM based compost as adsorbent, Ecotoxicol. Environ. Saf. 118 (2015) 177–182. https://doi.org/10.1016/j.ecoenv.2015.04.033.

[20] X. Hou, X. Tong, W. Dong, C. Dong, S. Shuang, Synchronous fluorescence determination of human serum albumin with methyl blue as a fluorescence probe, Spectrochim. Acta - Part A Mol. Biomol. Spectrosc. 66 (2007) 552–556. https://doi.org/10.1016/j.saa.2006.03.031.

[21] C. Sahoo, A.K. Gupta, Optimization of photocatalytic degradation of methyl blue using silver ion doped titanium dioxide by combination of experimental design and response surface approach, J. Hazard. Mater. 215–216 (2012) 302–310. https://doi.org/10.1016/j.jhazmat.2012.02.072.

[22] L. Han, S. Xue, S. Zhao, J. Yan, L. Qian, M. Chen, Biochar supported nanoscale iron particles for the efficient removal of methyl orange dye in aqueous solutions, PLoS One. 10 (2015) 1–15. https://doi.org/10.1371/journal.pone.0132067.

[23] D. Mirzaei, A. Zabardasti, Y. Mansourpanah, M. Sadeghi, S. Farhadi, Efficacy of Novel NaX/MgO–TiO2 Zeolite Nanocomposite for the Adsorption of Methyl Orange (MO) Dye: Isotherm, Kinetic and Thermodynamic Studies, J. Inorg. Organomet. Polym. Mater. 30 (2020) 2067–2080. https://doi.org/10.1007/s10904-019-01369-9.

[24] Z.X. Chen, X.Y. Jin, Z. Chen, M. Megharaj, R. Naidu, Removal of methyl orange from aqueous solution using bentonite-supported nanoscale zero-valent iron, J. Colloid Interface Sci. 363 (2011) 601–607. https://doi.org/10.1016/j.jcis.2011.07.057.

[25] E. Xingu-Contreras, G. García-Rosales, I. García-Sosa, A. Cabral-Prieto, Degradation of methyl orange using iron nanoparticles with/without support at different conditions, Microporous Mesoporous Mater. 292 (2020) 109782. https://doi.org/10.1016/j.micromeso.2019.109782.

[26] S. Arabi, M.R. Sohrabi, Removal of methylene blue, a basic dye, from aqueous solutions using nano-zerovalent iron, Water Sci. Technol. 70 (2014) 24–31. https://doi.org/10.2166/wst.2014.189.

[27] K. Badvi, V. Javanbakht, Enhanced photocatalytic degradation of dye contaminants with TiO2 immobilized on ZSM-5 zeolite modified with nickel nanoparticles, J. Clean. Prod. 280 (2021) 124518. https://doi.org/10.1016/j.jclepro.2020.124518.

[28] S. Zhu, X. Huang, D. Wang, L. Wang, F. Ma, Enhanced hexavalent chromium removal

performance and stabilization by magnetic iron nanoparticles assisted biochar in aqueous solution: Mechanisms and application potential, Chemosphere. 207 (2018) 50–59. https://doi.org/10.1016/j.chemosphere.2018.05.046.

[29] D. Fu, P.G. Keech, X. Sun, J.C. Wren, Iron oxyhydroxide nanoparticles formed by forced hydrolysis : dependence of phase composition on solution concentration, Phys. Chem. Chem. Phys. 13 (2011) 18523–18529. https://doi.org/10.1039/c1cp20188c.

[30] E. López-Fernández, C. Gómez-Sacedón, J. Gil-Rostra, J.P. Espinós, A.R. González-Elipe, F. Yubero, A. de Lucas-Consuegra, Ionomer-Free Nickel-Iron bimetallic electrodes for efficient anion exchange membrane water electrolysis, Chem. Eng. J. (2021) 133774. https://doi.org/10.1016/j.cej.2021.133774.

[31] Y. Yu, J. Peng, B. Liu, G. Chen, C. Srinivasakannan, Investigation on Preparation of Micro-Sized Hematite Powder from Hydrous Ferrous Sulfate Using Microwave and Conventional Heating, High Temp. Mater. Process. 32 (2013) 303–308. https://doi.org/10.1515/htmp-2012-0121.

[32] M. Rivero-Huguet, W.D. Marshall, Reduction of hexavalent chromium mediated by micro- and nano-sized mixed metallic particles, J. Hazard. Mater. 169 (2009) 1081–1087. https://doi.org/10.1016/j.jhazmat.2009.04.062.

[33] C. Jiao, Y. Cheng, W. Fan, J. Li, Synthesis of agar-stabilized nanoscale zero-valent iron particles and removal study of hexavalent chromium, Int. J. Environ. Sci. Technol. 12 (2015) 1603–1612. https://doi.org/10.1007/s13762-014-0524-0.

[34] B. Kakavandi, R.R. Kalantary, M. Farzadkia, A.H. Mahvi, A. Esrafili, A. Azari, A.R. Yari, A.B. Javid, Enhanced chromium (VI) removal using activated carbon modified by zero valent iron and silver bimetallic nanoparticles, J. Environ. Heal. Sci. Eng. 12 (2014) 1–10. https://doi.org/10.1186/s40201-014-0115-5.

[35] S. Li, T. You, Y. Guo, S. Yao, S. Zang, M. Xiao, Z. Zhang, Y. Shen, High dispersions of nano zero valent iron supported on biochar by one-step carbothermal synthesis and its application in chromate removal, RSC Adv. 9 (2019) 12428–12435. https://doi.org/10.1039/c9ra00304e.

[36] Y. He, J.F. Gao, F.Q. Feng, C. Liu, Y.Z. Peng, S.Y. Wang, The comparative study on the rapid decolorization of azo, anthraquinone and triphenylmethane dyes by zero-valent iron, Chem. Eng. J. 179 (2012) 8–18. https://doi.org/10.1016/j.cej.2011.05.107.

[37] P. Senthil Kumar, S.J. Varjani, S. Suganya, Treatment of dye wastewater using an ultrasonic aided nanoparticle stacked activated carbon: Kinetic and isotherm modelling, Bioresour. Technol. 250 (2018) 716–722. https://doi.org/10.1016/j.biortech.2017.11.097.

[38] P. Anju Rose Puthukkara, T. Sunil Jose, S. Dinoop lal, A.R. Puthukkara P, S. Jose T, D. lal S, Chitosan stabilized Fe/Ni bimetallic nanoparticles for the removal of cationic and anionic triphenylmethane dyes from water, Environ. Nanotechnology, Monit. Manag. 14 (2020) 100295. https://doi.org/10.1016/j.enmm.2020.100295.

[39] Y.H. Liou, S.L. Lo, C.J. Lin, W.H. Kuan, S.C. Weng, Chemical reduction of an unbuffered nitrate solution using catalyzed and uncatalyzed nanoscale iron particles, J. Hazard. Mater. 127 (2005) 102–110. https://doi.org/10.1016/j.jhazmat.2005.06.029.

[40] Y. Liu, G. V. Lowry, Effect of particle age (Fe0 content) and solution pH on NZVI reactivity: H2 evolution and TCE dechlorination, Environ. Sci. Technol. 40 (2006) 6085–6090. https://doi.org/10.1021/es060685o.

[41] A.D. Bokare, R.C. Chikate, C. V. Rode, K.M. Paknikar, Iron-nickel bimetallic nanoparticles for reductive degradation of azo dye Orange G in aqueous solution, Appl.

Catal. B Environ. 79 (2008) 270–278. https://doi.org/10.1016/j.apcatb.2007.10.033.

[42] Y.H. Liou, C.J. Lin, S.C. Weng, H.H. Ou, S.L. Lo, Selective decomposition of aqueous nitrate into nitrogen using iron deposited bimetals, Environ. Sci. Technol. 43 (2009) 2482–2488. https://doi.org/10.1021/es802498k.

[43] M.N. Morshed, N. Bouazizi, N. Behary, J. Guan, V. Nierstrasz, Stabilization of zero valent iron (Fe0) on plasma/dendrimer functionalized polyester fabrics for Fenton-like removal of hazardous water pollutants, Chem. Eng. J. 374 (2019) 658–673. https://doi.org/10.1016/j.cej.2019.05.162.

[44] A. Kumar, G. Sharma, M. Naushad, S. Thakur, SPION/β-cyclodextrin core-shell nanostructures for oil spill remediation and organic pollutant removal from waste water, Chem. Eng. J. 280 (2015) 175–187. https://doi.org/10.1016/j.cej.2015.05.126.

[45] Y. Ju, X. Liu, Z. Li, J. Kang, X. Wang, Y. Zhang, J. Fang, D.D. Dionysiou, Environmental application of millimetre-scale sponge iron (s-Fe0) particles (I): Pretreatment of cationic triphenylmethane dyes, J. Hazard. Mater. 283 (2015) 469–479. https://doi.org/10.1016/j.jhazmat.2014.09.051.

[46] L. Yong, G. Zhanqi, J. Yuefei, H. Xiaobin, S. Cheng, Y. Shaogui, W. Lianhong, W. Qingeng, F. Die, Photodegradation of malachite green under simulated and natural irradiation: Kinetics, products, and pathways, J. Hazard. Mater. 285 (2015) 127–136. https://doi.org/10.1016/j.jhazmat.2014.11.041.

[47] C. Berberidou, I. Poulios, N.P. Xekoukoulotakis, D. Mantzavinos, Sonolytic, photocatalytic and sonophotocatalytic degradation of malachite green in aqueous solutions, Appl. Catal. B Environ. 74 (2007) 63–72. https://doi.org/10.1016/j.apcatb.2007.01.013.

[48] G. Gao, A. Zhang, M. Zhang, J. Chen, Q. Zhang, Photocatalytic Degradation Mechanism of Malachite Green under Visible Light Irradiation over Novel Biomimetic Photocatalyst HMS-FePcs, Chinese J. Catal. 29 (2008) 426–430. https://doi.org/10.1016/S1872-2067(08)60043-1.

[49] G. Sharma, S. Bhogal, V.K. Gupta, S. Agarwal, A. Kumar, D. Pathania, G.T. Mola, F.J. Stadler, Algal biochar reinforced trimetallic nanocomposite as adsorptional/photocatalyst for remediation of malachite green from aqueous medium, J. Mol. Liq. 275 (2019) 499–509. https://doi.org/10.1016/j.molliq.2018.11.070.

[50] I. Owsik, B. Kolarz, The oxidation of hydroquinone to p-benzoquinone catalysed by Cu(II) ions immobilized on acrylic resins with aminoguanidyl groups: Part 1, J. Mol. Catal. A Chem. 178 (2002) 63–71. https://doi.org/10.1016/S1381-1169(01)00299-0.